A novel FFT-based phase field model for damage and cracking behavior of heterogeneous materials

Y.J. Cao, Wanqing Shen, Jian-Fu Shao, W. Wang

Version of Record: https://www.sciencedirect.com/science/article/pii/S0749641920300504
Manuscript_0153a080638fa65a4dfa26a28e4ef47e

A novel FFT-based phase field model for damage and cracking behavior of heterogeneous materials

Y.J. Cao[1], W.Q. Shen[1,2], J.F. Shao[1,2,*], W. Wang[1]

[1] *Key Laboratory of Ministry of Education for Geomechanics and Embankment Engineering, Hohai University, Nanjing 210098, China*
[2] *Univ. Lille, CNRS, Centrale Lille, UMR 9013 - LaMcube - Laboratoire de Mécanique, Multiphysique, Multi-échelle, F-59000 Lille, France*
**Corresponding author: jian-fu.shao@polytech-lille.fr*

Abstract

A novel numerical method is developed for three-dimensional modeling of damage and cracking in heterogeneous rock-like materials. Two key issues are addressed. For the first issue, influences of materials heterogeneities such as pores and inclusions on damage evolution and cracking processes are investigated by a homogenization approach with Fast Fourier Transform technique. For the second issue, the nucleation and propagation of cracks from diffuse damage evolution are formulated in Fourier space and described by a phase-field method. To do this, an efficient numerical procedure is developed for the stress-strain relationships and crack phase field propagation. A new elastic degradation function is proposed in order to describe a large range of cracking processes. A range of heterogeneous materials with different microstructure are generated and performed numerically to study effects of pores and inclusions on the damage evolution and cracking process in heterogeneous materials.

Keywords: Localized damage, Cracking, Phase field method, FFT-based homogenization, Heterogeneous materials, Rock-like materials

1. Introduction

From diffuse damage to localized cracks is the key issue of failures in most rock-like materials. For modeling the diffuse damage evolution, scalar or tensorial internal variables are usually adopted in macroscopic models to present the damage level. But they are not explicitly linked to the real distribution of micro-cracks in materials. The onset of localization occurs when the damage variables reach some critical values. After the localization, the related boundary values problem becomes ill-posed and suffers the suspicious mesh dependency. Therefore, in the context of macroscopic damage modeling, suitable regularization

methods should be used, for example the integral approaches (Pijaudier-Cabot and Bazant, 1987; Bazant and Pijaudier-Cabot, 1988; Duddu and Waisman, 2013; Reis et al., 2018) and also the gradient-damage approaches (Peerlings et al., 1996, 2001; Londono et al., 2017), etc. The damage variation of the point is controlled by a non-local driving force which is determined by an integration over a neighboring zone. Then an internal length is involved to describe micro-structural interactions. However, an inadequate treatment of damage interaction would result in non-physical damage initiation away from the crack tip in mode-I problems and incorrect failure pattern in shear band problem, especially near the free boundaries and discontinuities (Simone et al., 2004). In addition, the calculation of integration can be time consuming. In the recent decades, micromechanics-based damage models have also been established (Monchiet et al., 2012; Murari and Upadhyay, 2013; Dormieux and Kondo, 2016; Zhu and Shao, 2017). Macroscopic strains are directly related to displacement discontinuities across microscopic cracks. The effective elastic properties are determined by a rigorous homogenization technique (Zhu et al., 2009). In particular, the crack growth and frictional sliding has been physically coupled at the microscopic scale (Zhu and Shao, 2015; Zhao et al., 2018), which provides an excellent framework to describe diffuse damage with initial crack formation. However, the micromechanical-based methodologies mainly include cracking influence at the constitutive level through internal degradation of material parameters. The implementation of such models for localized cracking of practical structures analysis is not an easy task.

Numerical computational methods provide great advantages for various crack problems. For instance, the extended finite element method(XFEM) has become a popular tool to consider the discontinuities (Moës et al., 1999). It enables the accurate approximation of solutions with jumps within elements though additional enrichment functions of discontinuous and asymptotic fields. The combination of XFEM and other technique like the cohesive zone model (Wells and Sluys, 2001; Wang and Waisman, 2016; Li and Chen, 2017; Leclerc et al., 2018), discrete fracture model (Zeng et al., 2019, 2020) and damage mechanic model (Broumand and Khoei, 2013; Roth et al., 2015) have shown new solutions from diffuse damage to localized cracking behavior. However, a complex crack-tracking strategy is necessary to deal with the crack nucleation and propagation (Saloustros et al., 2019).

Recently, variationally based phase field methods (Francfort and Marigo, 1998; Bourdin et al., 2000) have overcome the limitations of the classical Griffith fracture theory. It employs a diffuse damage field to represent the discrete fracture surface. The quasi-static brittle cracking process is governed by the minimization of the total energy, which is a function of strain energy and fracture dissipation (Miehe et al., 2010b). The attractive feature of this method is its strong ability to simulate the complicated fracture process of nucleation,

propagation and branching both in 2D and 3D simulations without any additional criteria. Therefore, great efforts and extensions have also been done for brittle fracture (Borden et al., 2014; Msekh et al., 2015; Gerasimov and Lorenzis, 2016, 2019), quasi-brittle fracture (Nguyen et al., 2016; Wick, 2017; Ulloa et al., 2019), ductile fracture (Ambati et al., 2015; Borden et al., 2016; Miehe et al., 2016; Kienle et al., 2019), dynamic fracture (Borden et al., 2012; Nguyen and Wu, 2018; Ren et al., 2019) and multi-physicals fracturing problem (Miehe and Mauthe, 2016; Wilson and Landis, 2016; Zhuang et al., 2020; Nguyen et al., 2019) for various materials.

The cracking behavior of rock-like materials is a serious problem in rock engineering. The failure modes, however, are difficult to quantify or predict due to its complex physical and mechanical properties. Most importantly, the rock-like materials contains different kinds of heterogeneities at different scales. For instance, in clayey rocks, complex networks of pores and hard mineral inclusions such as carbonates and quartz are frequently observed (Shen et al., 2012). The deformation behavior of each heterogeneity is quite different. Macroscopic mechanical properties, including damage and cracking processes, are inherently influenced by the distribution and geometrical shape of pores and inclusions (Shen et al., 2018, 2019). So far, no analytical homogenization methods are able to explicitly deal with interactions between induced micro-cracks evolution and material heterogeneities (pores and inclusions). This is the challenge of the present study.

Two main issues have to be solved. The first one is to determine the influences of pores and mineral inclusions on the macroscopic responses of materials, depending on their spatial distribution, size and geometrical form. For most cases, it is not possible to establish analytical homogenization solutions. Numerical homogenization methods have successfully focused on estimating the effective mechanical behavior of heterogeneous materials (Feyel, 2003; Fish et al., 1999; Oskay and Fish, 2007; Geers et al., 2010; Meng et al., 2019a,b). All of these methods are following the classical framework of FEM from the view of numerical implementation. This has to require a careful mesh discretization for complex microstructure and high computational cost. In this study, a numerical homogenization approach with FFT technique will be developed for heterogeneous materials exhibiting elastic behavior with damage evolution. Recently, the development of Fast Fourier Transforms (FFT) homogenization is very quick. This kind of methods have initially been proposed for composite materials (Moulinec and Suquet, 1994, 1998), which was recently extended to rock-like materials (Li et al., 2018; Cao et al., 2018a). Without meshing, the FFT-based methods are particularly efficient to deal with materials with complex micro-structures and to investigate effects of size, shape and spatial distribution of heterogeneities. The second issue is the description of the change from diffuse to localized damage by considering interactions with

pores and inclusions. In the present study, we shall adopt the concept of phase-field method to describe naturally the evolution of diffuse damage, nucleation of cracks by damage localization and then propagation of cracks. This method will be extended and combined with the FFT-based homogenization procedure to deal with the cracking process in heterogeneous materials.

There are five principal parts in this work: the local mechanical behavior, damage evolution problem and general homogenization procedure of heterogeneous materials are first presented in Section 2. Then, the framework of Fourier-based phase field method (PFFT) is established in Section 3. Further in Section 4, a new algorithm for the decoupling strategy of coupling equations is described. The efficiency of this proposed PFFT model is assessed by a series of numerical studies for both homogeneous and heterogeneous materials in Section 5. Final, an experimental validation is provided in section 6 to show the prediction capacity of this PFFT method for heterogeneous materials.

2. Local formulations of heterogeneous materials

2.1. Formulation of phase field problem

For a clarity purpose, the essential principles of phase field method are recalled (Miehe et al., 2010b). An elastic solid Ω exhibiting an induced damage because of micro-cracks evolution is considered. With the increase of loading, the density of micro-cracks arrives at the critical state and therefor the onset of fractures begins due to the coalescence of micro-cracks into a narrow band. Discontinuous fields should be considered across those cracks, which is approximated in the phase field approach through a regularized one by introducing an auxiliary damage field: $d(\boldsymbol{x}_p, t) \in [0, 1]$, seen as an internal variable of damage state. The material is intact with $d = 0$ and is totally broken when $d = 1$. It is shown that the crack state can be calculated by solving the Euler variational problem (Miehe et al., 2010a):

$$d(\boldsymbol{x}_p, t) = Arg\left\{\inf_{d\subset\Omega}\Pi_d^{\bar{\tau}}(d)\right\} \tag{1}$$

It is assumed that the evolution of crack field is time-dependent. The total energy functional $\Pi_d^{\bar{\tau}}(d)$ is then composed of three parts: the energy needed for crack creation, the energy related to time-dependent damage and that to the instantaneous damage:

$$\Pi_d^{\bar{\tau}}(d) = \int_\Omega [g_c\gamma_d(d, \nabla d) + \frac{\eta}{2\bar{\tau}}(d - d_n)^2 + \partial_d\psi(\boldsymbol{\varepsilon}, d)]dV \tag{2}$$

In this relation, g_c is the crack surface energy. η is the viscosity parameter that controls the time-dependent evolution of d. The time derivative is approximated by the difference over

the time interval such $\dot{d} := (d - d_n)/\bar{\tau}$ with $\bar{\tau} := (t - t_n)$. $\psi(\boldsymbol{\varepsilon}, d)$ is the elastic strain energy. Further, the function γ_d denotes the crack surface density per unit volume which can be expressed as:

$$\gamma_d(d, \nabla d) = \frac{1}{2l_c}d^2 + \frac{l}{2}|\nabla d|^2 \tag{3}$$

in which l_c denotes the length scale parameter which defines the thickness of localization bands. The variational principle leads to the following partial differential equations:

$$g_c l\nabla^2 d - \frac{g_c}{l_c}d = \eta\dot{d} + g'(d)\psi_0(\boldsymbol{\varepsilon}) \tag{4}$$

where the elastic strain energy of damaged material will be decomposed into two terms: the function $g(d)$ defines the degradation of elastic properties by damage while $\psi_0(\boldsymbol{\varepsilon})$ is the intact energy. On the other, to consider the irreversible variation of crack field during complex loading history including unloading and reloading, the following energy history function $\mathcal{H}$ is introduced to represent the maximum reference value of the elastic strain energy of undamaged material $\psi(\boldsymbol{\varepsilon})$ (Miehe et al., 2010a) as:

$$\mathcal{H}(\boldsymbol{x}_p, t) = \max_{\boldsymbol{x}_p \in [0,t]} \psi_0^+(\boldsymbol{\varepsilon}, \boldsymbol{x}_p) \tag{5}$$

Therefore, the crack phase field is finally determined by solving the following equation:

$$g_c l\nabla^2 d - \frac{g_c}{l_c}d = \eta\dot{d} + g'(d)\mathcal{H} \tag{6}$$

2.2. Stress-strain relation of damaged material

According to the displacement field $\boldsymbol{u}(\boldsymbol{x}_p, t)$ at the location $\boldsymbol{x}_p \in \Omega$ at time t, the corresponding strain tensor can be calculated in the framework of small strains $\boldsymbol{\varepsilon}(\boldsymbol{x}_p, t) = 1/2(\nabla\boldsymbol{u}(\boldsymbol{x}_p, t) + \nabla\boldsymbol{u}(\boldsymbol{x}_p, t)^T)$ For convenience, the strain tensor is divided into an tensile part (noted by positive sign) and a compressive part (noted by negative sign) such as:

$$\boldsymbol{\varepsilon} = \boldsymbol{\varepsilon}^+ + \boldsymbol{\varepsilon}^- \tag{7}$$

The two parts of strain tensor are calculated by using a spectral decomposition:

$$\boldsymbol{\varepsilon}^\pm = \sum_{i=1}^{N} \langle\varepsilon_i\rangle^\pm \boldsymbol{n}_i \otimes \boldsymbol{n}_i \tag{8}$$

where $\boldsymbol{\varepsilon}_i$ are the eigenvalues of strain tensor and $\boldsymbol{n}_i$ are the corresponding eigenvectors. The bracket symbol denotes $\langle a\rangle^\pm = (a \pm |a|)/2$. Then, the elastic strain energy function of undamaged materials ψ_0 is also decomposed into two parts: negative one ψ_0^- and positive

one ψ_0^+. Further, it is assumed that the induced damage affects only the positive part ψ_0^+. Therefore, the elastic strain energy function of damaged materials is given by:

$$\psi(\boldsymbol{\varepsilon}, d) = \psi_0^-(\boldsymbol{\varepsilon}) + [g(d) + k]\psi_0^+(\boldsymbol{\varepsilon}) \tag{9}$$

In this work, only isotropic materials are studied. Thus, the elastic strain energy functions are given by:

$$\psi_0^{\pm}(\boldsymbol{\varepsilon}) = \mu(\boldsymbol{\varepsilon}^{\pm} : \boldsymbol{\varepsilon}^{\pm}) + \frac{\lambda}{2}\langle tr[\boldsymbol{\varepsilon}]\rangle_{\pm}^2 \tag{10}$$

in which λ and μ denote respectively the Lame's elastic constants of undamaged materials. The stress-strain relations of damaged materials are derived from the elastic strain energy function (9):

$$\begin{aligned} \boldsymbol{\sigma} &= \partial_{\boldsymbol{\varepsilon}}\psi(\boldsymbol{\varepsilon}, d) \\ &= [\lambda\langle tr(\boldsymbol{\varepsilon})\rangle_{-}\boldsymbol{I} + 2\mu\boldsymbol{\varepsilon}_{-}] + (g(d) + k)[\lambda\langle tr(\boldsymbol{\varepsilon})\rangle_{+}\boldsymbol{I} + 2\mu\boldsymbol{\varepsilon}_{+}] \end{aligned} \tag{11}$$

in which $\boldsymbol{I}$ is the second-order unit tensor.

The elastic modulus of damaged materials are deteriorated with the evolution of damage. This deterioration is characterized here by the function $g(d)$, which has the following quadratic form in the classical phase field method (Miehe et al., 2010b; Borden et al., 2012; Vignollet et al., 2014):

$$g_1(d) = (1 - d)^2 \tag{12}$$

This function generally leads to a sharp reduction of elastic stiffness prior to the crack propagation and then produces a typical brittle failure process. To avoid this drawback, alternative degradation functions have also appeared in the literatures, such as the cubic form (Borden, 2012), energetic degradation function (Wu, 2017), and so on. As illustrated by Kuhn et al. (2015), the material response remains linear almost until the onset of fracture for the cubic and the quadratic degradation functions. Their differences rest with strain or stress state at which crack propagation occurs, and also with the amount of stiffness reduction observed prior to the onset of fracture. Actually, the selection of degradation function depends on the mechanical properties of materials. For example, the cubic degradation function has an advantage that less damage occurs prior to crack initiation (Borden, 2012). So it is more suitable for brittle fracture as it yields a more abrupt failure. For heterogeneous rock-like materials, the nonlinear deformation before the onset of fracture is significant. With the increase of confining stress, the material failure changes from brittle to ductile. Therefore, the failure process is progressive. This phenomenon can be clarified by experimental observations in large numbers of literatures (Okubo and Fukui, 1996; Martin and Chandler, 1994; Tang et al., 2019).

For this reason, inspired by the work of Wu (2017), a new degradation function is defined here to describe a large range of failure processes:

$$g_2(d) = (1 - \alpha(d))^2 = (1 - \frac{(A-1)d^2 + Bd}{Ad^2 + (B-2)d + 1})^2 \tag{13}$$

In this function, parameter A and B control the degradation kinetics and meet the conditions $A \geq 1$ and $B > 0$. Further, as for the classical function $g_1(d)$, the new function also has the basic properties such that $g_2(1) = 0$, $g_2(0) = 1$, and $g_2'(1) = 0$. It is noted that a similar parametric degradation function is also adopted by Sargado et al. (2018) and Lu and Chen (2020) to increase the accuracy of phase-field models. For heterogeneous materials studied in this work, the parameters A and B are related to the material properties of the solid matrix. They can be identified by a series of triaxial compression and extension tests of rock samples. Based on the experimentally obtained macroscopic failure strength envelope line and using the parameter inversion analysis, the optimal parameters of A and B can be obtained by fitting the simulated strength envelope line with the experimental result. It is worth to note that this function is still empirical but provides more possibility of phase field evolution for heterogeneous materials.

Figure 1(a) and 1(b) show the influences of these two parameters on the degradation function. For a small value of A (with a constant B) or B (with a constant A), one gets a slow evolution of degradation function with the damage parameter d. This should lead to a progressive or ductile failure process. More detailed discussions will be given later on influences of these parameters on macroscopic responses through parametric studies.

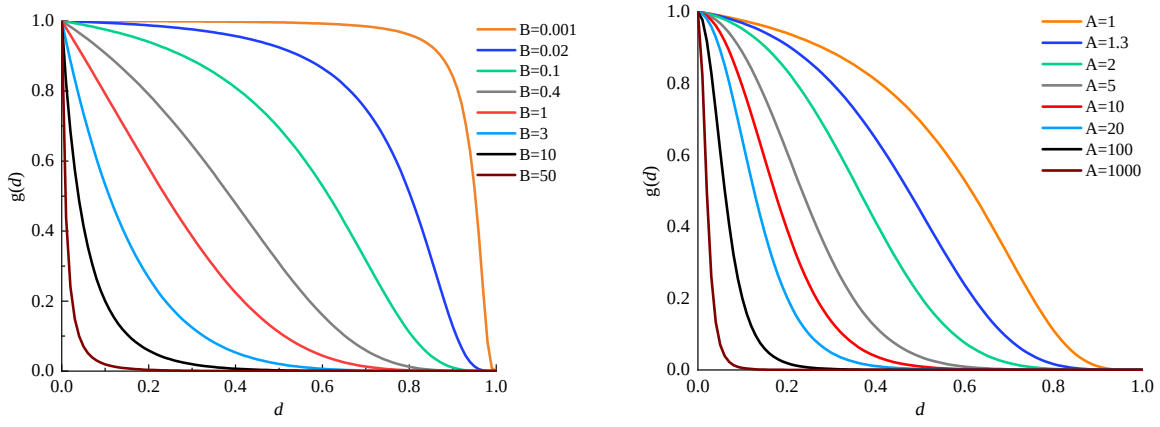

(a) $A = 1$ (b) $B = 0.1$

Figure 1: The evolution of degradation function for different values of A and B

2.3. Homogenization procedure of heterogeneous material

One considers here heterogeneous materials with a periodic micro-structure and heterogeneities of inclusions and pores. A cubic unit cell is selected as the representative volume element (RVE). The local stress and strain fields inside this unit cell are not uniform. By introducing a fluctuation field of displacement $\boldsymbol{u}^*(\boldsymbol{x}_p)$ (Moulinec and Suquet, 1994, 1998), the local strain field $\boldsymbol{\varepsilon}(\boldsymbol{u}(\boldsymbol{x}_p))$ is composed of an average strain field $\boldsymbol{E}$ and a fluctuation field $\boldsymbol{\varepsilon}(\boldsymbol{u}^*(\boldsymbol{x}_p))$:

$$\boldsymbol{\varepsilon}(\boldsymbol{u}(\boldsymbol{x}_p)) = \boldsymbol{E} + \boldsymbol{\varepsilon}(\boldsymbol{u}^*(\boldsymbol{x}_p)), \tag{14}$$

According to the prescribed deformation loading $\boldsymbol{E}$, the goal in this study is to calculate the macroscopic stress $\boldsymbol{\Sigma}$ by considering the local constitutive relations. This comes to solve the following governing equations:

$$\begin{cases} \boldsymbol{\sigma}(\boldsymbol{x}_p) = (g(d)+k)[\lambda\langle tr(\boldsymbol{\varepsilon}(\boldsymbol{x}_p))\rangle_+\boldsymbol{I} + 2\mu\boldsymbol{\varepsilon}_+(\boldsymbol{x}_p)] + [\lambda\langle tr(\boldsymbol{\varepsilon}(\boldsymbol{x}_p))\rangle_-\boldsymbol{I} + 2\mu\boldsymbol{\varepsilon}_-(\boldsymbol{x}_p)] & \forall \boldsymbol{x}_p \in \Omega_s \\ div\boldsymbol{\sigma}(\boldsymbol{x}_p) = 0 & \forall \boldsymbol{x}_p \in \Omega, u^*\#, \boldsymbol{\sigma}\cdot n - \# \\ \boldsymbol{\varepsilon}(\boldsymbol{x}_p) = \varepsilon(\boldsymbol{u}^*(\boldsymbol{x}_p)) + \boldsymbol{E} & \forall \boldsymbol{x}_p \in \Omega \\ g_c l\nabla^2 d - \dfrac{g_c}{l_c} d = \eta\dot{d} + g'(d)\mathcal{H}(\boldsymbol{\varepsilon}) \end{cases} \tag{15}$$

This problem is solved here by using the numerical homogenization approach with the FFT technique as suggested in Moulinec and Suquet (1998). To this end, an auxiliary problem considering a reference homogeneous linear elastic material with the elastic stiffness $\mathbb{C}_0$ and subjected to a polarization field $\boldsymbol{\tau}(t, \boldsymbol{x}_p)$ is introduced to determine the fluctuation strain field. As the time-dependent behavior is considered in this work, the polarization stress is then defined as $\boldsymbol{\tau}(t, \boldsymbol{x}_p) = \boldsymbol{\sigma}(t, \boldsymbol{x}_p) - \mathbb{C}_0 : \boldsymbol{\varepsilon}(t, \boldsymbol{x}_p)$ (Cao et al., 2018a). Finally the first three relations can be reduced to the periodic Lippmann-Schwinger equation:

$$\boldsymbol{\varepsilon}(t, \boldsymbol{x}_p) = \boldsymbol{E} - \boldsymbol{\Gamma}_0(\boldsymbol{x}_p) * \boldsymbol{\tau}(t, \boldsymbol{x}_p) \tag{16}$$

in which Γ^0 denotes the Green's operator, which allows to determine the fluctuation strain field induced by the polarization stress at each point $\boldsymbol{x}_p$. Once the local mechanical fields and crack phase field are determined, the macroscopic stress $\boldsymbol{\Sigma}$ is simply determined by the following relationship:

$$\boldsymbol{\Sigma} = \frac{1}{\Omega}\int_\Omega \boldsymbol{\sigma}(\boldsymbol{x}_p, t) dV \tag{17}$$

In addition, to qualities the macroscopic damage evolution during the whole cracking process, an overall damage variable D is also calculated as follows:

$$D = \frac{1}{\Omega}\int_\Omega d(\boldsymbol{x}_p, t) dV \tag{18}$$

3. Formulation of Fourier Transform-based phase field method (PFFT)

3.1. Mechanical solution in Fourier space

The local problems are defined in the previous section for determining respectively the mechanical fields by (16) and the damage one by (6). In most previous studies, the crack phase field method is generally coupled within a finite element code to derive sequently solutions of damage phase field d and of displacement field $\boldsymbol{u}$. However, for heterogeneous materials considered here, irregular and fine meshes are needed to represent heterogeneities. This generally constitutes a delicate task and leads to an expensive calculation cost, especially for three dimensional problems.

The basic scheme of FFT-based numerical homogenization has been proposed for composites materials by Moulinec and Suquet (1994, 1998); Michel et al. (2001). Its efficiency has been ameliorated by Eyre and Milton (1999); Zeman et al. (2010); Brisard and Dormieux (2010); Moulinec and Silva (2014); Kabel et al. (2014) with different algorithms for highly contrasted materials. The basic scheme is adopted here for the simplicity of numerical implementation. Due to the non-linearity of material behavior, the total loading time T_N is divided into N time increments such as $\Delta t = t_{n+1} - t_n$ with $n \in [0, N-1]$. The values of local stresses and strains at the state t_{n+1} is calculated based on the ones at t_n. To this end, the governing equation (16) is reformulated in Fourier space based on the convolution theorem, that is:

$$\hat{\boldsymbol{\varepsilon}}(t_{n+1}, \boldsymbol{\xi}) = -\hat{\boldsymbol{\Gamma}}^{\mathbf{0}}(\boldsymbol{\xi}) : \hat{\boldsymbol{\tau}}(t_{n+1}, \boldsymbol{\xi}) \quad \text{with} \quad \boldsymbol{\xi} \neq \mathbf{0}; \quad \hat{\varepsilon}(\mathbf{0}) = \boldsymbol{E} \tag{19}$$

in the above equation the symbol $\hat{}$ denotes the variables in Fourier space. $\boldsymbol{\xi}$ are the coordinates, and $\hat{\varepsilon}(t_{n+1}, \boldsymbol{\xi})$ the local strain at t_{n+1} in Fourier space. The operator $\boldsymbol{\Gamma^0}$ is explicitly given by:

$$\hat{\Gamma}^0_{khij}(\boldsymbol{\xi}) = \frac{1}{4\mu^0|\boldsymbol{\xi}|^2}(\delta_{ki}\xi_h\xi_j + \delta_{hi}\xi_k\xi_j + \delta_{kj}\xi_h\xi_i + \delta_{hj}\xi_k\xi_i) - \frac{\lambda^0 + \mu^0}{\mu^0(\lambda^0 + 2\mu^0)}\frac{\xi_i\xi_j\xi_k\xi_h}{|\boldsymbol{\xi}|^4} \tag{20}$$

In this expression, μ^0 and λ^0 are the two elastic constants of a reference material. Further, the polarization stress tensor $\hat{\boldsymbol{\tau}}(t_{n+1}, \boldsymbol{\xi})$ in (19) is replaced by $\hat{\boldsymbol{\sigma}}(t_{n+1}, \boldsymbol{\xi}) - \boldsymbol{C}_0 : \hat{\varepsilon}(t_{n+1}, \boldsymbol{\xi})$, so that an iterated form of equation (19) can be derived:

$$\hat{\boldsymbol{\varepsilon}}^{i+1}(t_{n+1}, \boldsymbol{\xi}) = \hat{\boldsymbol{\varepsilon}}^{i}(t_{n+1}, \boldsymbol{\xi}) - \hat{\boldsymbol{\Gamma}}^{0}(\boldsymbol{\xi}) : \hat{\boldsymbol{\sigma}}(t_{n+1}, \boldsymbol{\xi}) \qquad \forall \boldsymbol{\xi} \neq \mathbf{0}, \hat{\boldsymbol{\varepsilon}}(\mathbf{0}) = \boldsymbol{E}. \tag{21}$$

As introduced in Moulinec and Suquet (1994, 1998), a fixed point algorithm can be adopted to operate this iterated formulation. This algorithm has also been applied to rock-like materials with inelastic behavior Li et al. (2018); Cao et al. (2018a,b). Its efficiency and accuracy have been verified by the finite element results.

3.2. Phase field solution in Fourier space

The crack damage field d at step t_{n+1} is also solved in Fourier space after the solution of mechanical fields. In order to consider the different forms of degradation function, the governing equation of crack phase field is written in the following general form:

$$\mathcal{A}(t_{n+1}, \boldsymbol{x}_p) d(t_{n+1}, \boldsymbol{x}_p) - \nabla^2 d(t_{n+1}, \boldsymbol{x}_p) = \mathcal{B}(t_{n+1}, \boldsymbol{x}_p) \tag{22}$$

with

$$\mathcal{A}(t_{n+1}, \boldsymbol{x}_p) = \frac{1}{l^2(\boldsymbol{x}_p)} + \frac{\eta}{g_c(\boldsymbol{x}_p) l_c(\boldsymbol{x}_p) \Delta t} + \frac{2\alpha(d)\alpha'(d)\mathcal{H}(t_{n+1}, \boldsymbol{x}_p)}{g_c(\boldsymbol{x}_p) l_c(\boldsymbol{x}_p) d(t_{n+1}, \boldsymbol{x}_p)} \tag{23}$$

$$\mathcal{B}(t_{n+1}, \boldsymbol{x}_p) = \frac{\eta d(t_n, \boldsymbol{x}_p)}{g_c(\boldsymbol{x}_p) l_c(\boldsymbol{x}_p) \Delta t} + \frac{2\alpha'(d)\mathcal{H}(t_{n+1}, \boldsymbol{x}_p)}{g_c(\boldsymbol{x}_p) l_c(\boldsymbol{x}_p)} \tag{24}$$

When $\alpha(d) = d$, one gets the case of the classical degradation function $g_1(d)$. Following the idea of Chen et al. (2019), a homogeneous variable $\mathcal{A}_0$ is introduced at the two sides of Equation (22):

$$\mathcal{A}_0 d(t_{n+1}, \boldsymbol{x}_p) - \nabla^2 d(t_{n+1}, \boldsymbol{x}_p) = \mathcal{B}(t_{n+1}, \boldsymbol{x}_p) - (\mathcal{A}(t_{n+1}, \boldsymbol{x}_p) - \mathcal{A}_0) d(t_{n+1}, \boldsymbol{x}_p) \tag{25}$$

As studied by Chen et al. (2019), the following form of A_0 is selected to provide a fast convergence rate:

$$\mathcal{A}_0 = \frac{\max \mathcal{A}(t_{n+1}, \boldsymbol{x}_p) + \min \mathcal{A}(t_{n+1}, \boldsymbol{x}_p)}{2} \tag{26}$$

Further, the equation (25) contains differential operators that are nonlocal. The Fast Fourier transform technique provides a simple and efficient way to transform the nonlocal differential operations in real space into local in Fourier space (Sharma et al., 2018, 2019). Hence, in Fourier space, the equation (25) becomes:

$$(\mathcal{A}_0 + \|\boldsymbol{\xi}\|^2) \hat{d}(t_{n+1}, \boldsymbol{\xi}) = \mathcal{FFT}(T(t_{n+1}, \boldsymbol{x}_p, d)) \tag{27}$$

with

$$T(t_{n+1}, \boldsymbol{x}_p, d) = \mathcal{B}(t_{n+1}, \boldsymbol{x}_p) - (\mathcal{A}(t_{n+1}, \boldsymbol{x}_p) - \mathcal{A}_0) d(t_{n+1}, \boldsymbol{x}_p) \tag{28}$$

Then one gets the crack phase field in Fourier space:

$$\hat{d}(t_{n+1}, \boldsymbol{\xi}) = \hat{\phi}(t_{n+1}, \boldsymbol{\xi}, d) = \frac{\mathcal{FFT}(T(t_{n+1}, \boldsymbol{x}_p, d))}{(\mathcal{A}_0 + \|\boldsymbol{\xi}\|^2)} \tag{29}$$

With the inverse of FFT, an implicit expression of the phase field in real space:

$$d(t_{n+1}, \boldsymbol{x}_p) = \phi(t_{n+1}, \boldsymbol{x}_p, d) = \mathcal{FFT}^{-1} \left\{ \frac{\mathcal{FFT}(T(t_{n+1}, \boldsymbol{x}_p, d))}{(\mathcal{A}_0 + \|\boldsymbol{\xi}\|^2)} \right\} \tag{30}$$

In this way, the solution of crack phase field is transformed to find the root of a simple one-dimensional nonlinear equation. The so-called Steffensen's method is used in this work. This method is a combination of fixed-point iteration and the Aitken's method, which can achieve quadratic convergence (Conte and De Boor, 2018). With this method in hand, d is calculated by the following iterate form:

$$d^{i+1}(t_{n+1}, \boldsymbol{x}_p) = d^i(t_{n+1}, \boldsymbol{x}_p) - \frac{(\phi(t_{n+1}, \boldsymbol{x}_p, d^i) - d^i(t_{n+1}, \boldsymbol{x}_p))^2}{d^i(t_{n+1}, \boldsymbol{x}_p) - 2\phi(t_{n+1}, \boldsymbol{x}_p, d^i) + \phi(t_{n+1}, \boldsymbol{x}_p, \phi(t_{n+1}, \boldsymbol{x}_p, d^i))} \tag{31}$$

Further, the following convergence criterion is adopted:

$$\|d^{i+1}(t_{n+1}, \boldsymbol{x}_p) - d^i(t_{n+1}, \boldsymbol{x}_p)\|_2 \leq \varepsilon_{tol} \tag{32}$$

in which $\|\cdot\|_2$ denotes the L-2 norm; ε_{tol} is the convergence error. In this paper, $\varepsilon_{tol} = 1 \times 10^{-4}$ is adopted for all calculations.

4. Numerical implementation

The numerical implementation of the proposed algorithms is now presented. The phase field evolution depends on the history function $\mathcal{H} = \mathcal{H}(t_{n+1}, \boldsymbol{x}_p)$. This function establishes a direct link between the damage field and mechanical fields. To establish an algorithmic decoupling strategy, an approximation has been introduced for the calculation of the history function by Chen et al. (2019). In their work, an explicit one-pass staggered algorithm was introduced for solving the coupling problem, which closely relaying on a history field $\mathcal{H}(t, \boldsymbol{x}_p)$. Its values at t_{n+1} was calculated with the known displacement field at t_n so that $\mathcal{H}(t_{n+1}, \boldsymbol{x}_p) = \max_{x_p \in [0, t_n]} \psi_0^+(\boldsymbol{\varepsilon}, \boldsymbol{x}_p)$. This idea mainly follows the study of Miehe et al. (2010a). Thus the mechanical and phase field subproblems are respectively solved by one step. Despite the one-pass staggered approach enjoys great popularity due to its unconditional robustness, it requires extremely small time increment, nearly 10^{-7} (Wu and Huang, 2020).

In this work, this approximation is not used and the history function is calculated according to the maximum tensile strain energy achieved during the whole loading process until the current time step, namely $\mathcal{H}(t_{n+1}, \boldsymbol{x}_p) = \max_{x_p \in [0, t_{n+1}]} \psi_0^+(\boldsymbol{\varepsilon}, \boldsymbol{x}_p)$. This choice better describes the crack phase field evolution and its coupling those of mechanical fields at all time steps.

However, it is not easy to establish a direct coupling approach associated with the unknown fields $\boldsymbol{\varepsilon}$ and d. Instead, an iterative staggered method is proposed to decouple two linear subproblems given in equations (21) and (31). The requires to alternately fix the values of $\boldsymbol{\varepsilon}$ and d during the iteration process. Similar strategies have also been presented in recent some works, for instance (Miehe et al., 2010a; Shanthraj et al., 2016; Molnár and

Gravouil, 2017). Accordingly, the iterative staggered decoupling process is proposed in Algorithm 1. The present algorithm is quite different with the one proposed by Chen et al. (2019) who implemented an explicit fixed phase field value into the FFT homogenization framework for each iteration of strain field. For the new proposed algorithm, the phase field is solved implicitly and related to the iterate stain field during the stress balance process.

Algorithm 1: Algorithm for Fourier-based phase field method

Input: $\boldsymbol{\varepsilon}(t_n, \boldsymbol{x}_p),\ \Delta\boldsymbol{E}(t_{n+1}),\ d(t_n, \boldsymbol{x}_p),\ \Delta t_{n+1}$

Output: $\boldsymbol{E}(t_{n+1}),\ \boldsymbol{\Sigma}(t_{n+1}),\ d(t_{n+1}, \boldsymbol{x}_p)$

Initialization:$t_{n+1} = t_n + \Delta t_{n+1}$; $\boldsymbol{\varepsilon}^0(t_{n+1}, \boldsymbol{x}_p) = \boldsymbol{\varepsilon}(t_n, \boldsymbol{x}_p) + \Delta\boldsymbol{E}(t_{n+1}), \forall \boldsymbol{x}_p \in \Omega$;

$d^{0,0}(t_{n+1}, \boldsymbol{x}_p) = d(t_n, \boldsymbol{x}_p)$, and compute $\mathcal{H}(\boldsymbol{\varepsilon}^0)$;

while $(\|d^{0,i+1} - d^{0,i}\| \geq \epsilon_{tol})$ **do**

  Calculate $T^0(t_{n+1}, \boldsymbol{x}_p, d^{0,i}), \mathcal{A}_0^0$;

  $\phi(t_{n+1}, \boldsymbol{\xi}, d^{0,i}) = \mathcal{FFT}^{-1}(\dfrac{\mathcal{FFT}(T^0(t_{n+1}, \boldsymbol{x}_p, d^{0,i}))}{\mathcal{A}_0^0 + \|\boldsymbol{\xi}\|^2})$;

  $d^{0,i+1}(t_{n+1}, \boldsymbol{x}_p) = d^{0,i} - \dfrac{(\phi(t_{n+1}, \boldsymbol{x}_p, d^{0,i}) - d^{0,i})^2}{d^{0,i} - 2\phi(t_{n+1}, \boldsymbol{x}_p, d^{0,i}) + \phi(t_{n+1}, \boldsymbol{x}_p, \phi(t_{n+1}, \boldsymbol{x}_p, d^{0,i}))}$;

  $i = i + 1$;

end

$d^0(t_{n+1}, \boldsymbol{x}_p) = d^{0,i+1}(t_{n+1}, \boldsymbol{x}_p)$;

$\boldsymbol{\sigma}^0(t_{n+1}, \boldsymbol{x}_p) = [g(d^0(t_{n+1}, \boldsymbol{x}_p)) + k][\lambda\langle tr(\boldsymbol{\varepsilon}^0)\rangle_+\boldsymbol{I} + 2\mu\boldsymbol{\varepsilon}_+^0] + [\lambda\langle tr(\boldsymbol{\varepsilon}^0)\rangle_-\boldsymbol{I} + 2\mu\boldsymbol{\varepsilon}_-^0]$;

for $j = 0 : N_{iter}$ **do**

  The initial iterate step $\boldsymbol{\sigma}^0(t_{n+1})$, $\boldsymbol{\varepsilon}^0(t_{n+1})$ and $d^0(t_{n+1})$ at each point $\boldsymbol{x}_p$ are known ;

  $\hat{\boldsymbol{\sigma}}^j(t_{n+1}, \boldsymbol{\xi}_p) = \mathcal{FFT}(\boldsymbol{\sigma}^j(t_{n+1}, \boldsymbol{x}_p))$;

  Convergence test $\epsilon_{error} = \frac{(\langle\|\boldsymbol{\xi}\cdot\hat{\boldsymbol{\sigma}}^j(\boldsymbol{\xi})\|^2\rangle)^{1/2}}{\|\hat{\boldsymbol{\sigma}}^j(\boldsymbol{0})\|}$;

  if $\epsilon_{error} < 10^{-4}$ **then**

    Return;

  else

    $\hat{\boldsymbol{\varepsilon}}^{j+1}(t_{n+1}, \boldsymbol{\xi}) = \hat{\boldsymbol{\varepsilon}}^j(t_{n+1}, \boldsymbol{\xi}) - \hat{\Gamma}^0(\boldsymbol{\xi}) : \hat{\boldsymbol{\sigma}}^j(t_{n+1}, \boldsymbol{\xi}) \qquad \forall \boldsymbol{\xi}_p \neq \boldsymbol{0}, \quad \hat{\boldsymbol{\varepsilon}}^{j+1}(\boldsymbol{0}) = \boldsymbol{E}(t_{n+1})$;

    $\boldsymbol{\varepsilon}^{j+1}(t_{n+1}, \boldsymbol{x}_p) = \mathcal{FFT}^{-1}(\hat{\boldsymbol{\varepsilon}}^{j+1}(t_{n+1}, \boldsymbol{\xi}))$ and compute $\mathcal{H}(\boldsymbol{\varepsilon}^{j+1})$;

    while $(\|d^{j+1,i+1} - d^{j+1,i}\| \geq \epsilon_{tol})$ **do**

      Calculate $T^{j+1}(t_{n+1}, \boldsymbol{x}_p, d^{j+1,i}), \mathcal{A}_0^j$;

      $\phi = \mathcal{FFT}^{-1}(\dfrac{\mathcal{FFT}(T^{j+1}(t_{n+1}, \boldsymbol{x}_p, d^{j+1,i}))}{\mathcal{A}_0^j + \|\boldsymbol{\xi}\|^2})$;

      $d^{j+1,i+1} = d^{j+1,i} - \dfrac{(\phi(t_{n+1}, \boldsymbol{x}_p, d^{j+1,i}) - d^{j+1,i})^2}{d^{j+1,i} - 2\phi(t_{n+1}, \boldsymbol{\xi}, d^{j+1,i}) + \phi(t_{n+1}, \boldsymbol{x}_p, \phi(t_{n+1}, \boldsymbol{x}_p, d^{j+1,i}))}$;

      $i = i + 1$;

    end

    $d^{j+1}(t_{n+1}, \boldsymbol{x}_p) = d^{j+1,i+1}(t_{n+1}, \boldsymbol{x}_p)$;

    $\boldsymbol{\sigma}^{j+1}(t_{n+1}, \boldsymbol{x}_p) = [g(d^{j+1}(t_{n+1}, \boldsymbol{x}_p))+k][\lambda\langle tr(\boldsymbol{\varepsilon}^{j+1})\rangle_+\boldsymbol{I}+2\mu\boldsymbol{\varepsilon}_+^{j+1}]+[\lambda\langle tr(\boldsymbol{\varepsilon}^{j+1})\rangle_-\boldsymbol{I}+2\mu\boldsymbol{\varepsilon}_-^{j+1}]$;

    $j = j + 1$;

  end

end

Calculate the macroscopic stress $\bar{\boldsymbol{\Sigma}}_{iter}(t_{n+1}) = \frac{1}{|\Omega|}\int_\Omega \boldsymbol{\sigma}(t_{n+1}, \boldsymbol{x}_p)dV$

In addition, the basic-FFT scheme presented in Algorithm 1 just considers the prescribed macroscopic strain tensor as input data. For a large number of problems, both macroscopic stresses and strains can be prescribed on different parts of boundary. As an example, for a

conventional triaxial compression test, the macroscopic boundary conditions are given by:

$$\begin{aligned} &\boldsymbol{\Sigma}_0^{11} = \Sigma_0, \ \boldsymbol{E}_0^{12} = 0, \quad \boldsymbol{E}_0^{13} = 0 \\ &\boldsymbol{\Sigma}_0^{21} = 0, \quad \boldsymbol{\Sigma}_0^{22} = \Sigma_0, \ \boldsymbol{E}_0^{23} = 0 \\ &\boldsymbol{\Sigma}_0^{31} = 0, \quad \boldsymbol{E}_0^{32} = 0, \quad \boldsymbol{E}_0^{33} = E_{33} \end{aligned} \tag{33}$$

For triaxial test, the macroscopic stress is firstly constrained to a given value Σ_0 in the e_1, e_2 and e_3 directions. This value corresponds to the confining stress. Then a macroscopic strain is applied in the direction e_3. We note that the strain boundary condition in the e_1 and e_2 directions is free to deform with fixed macroscopic stress while the given strain loading is prescribed in the direction e_3. This kind of mixed boundary conditions implies an additional macroscopic stress balance condition to be introduced to verify the prescribed confining stress in the e_1 and e_2 directions. To this end, the so-called penalty technique is adopted here by adding a large number (eg. 10^{30}) to the main diagonal term of the reference stiffness matrix $\boldsymbol{C}_0$ corresponding to the prescribed strain direction. As a consequence, the Newton-Raphson's method is adopted here to consider the mixed boundary condition. The Algorithm 2 shows the modified procedure.

Algorithm 2: Newton iteration algorithm

Input: $\boldsymbol{\varepsilon}(t_n, \boldsymbol{x}_p)$, $\Delta \boldsymbol{E}^{BC}(t_{n+1})$, $\boldsymbol{\Sigma}^{BC}$, Δt_{n+1}
Output: $\boldsymbol{E}(t_{n+1})$, $\boldsymbol{\Sigma}(t_{n+1})$, $d(t_{n+1}, \boldsymbol{x}_p)$, $D(t_{n+1}, \boldsymbol{x}_p)$
Initialization: $t_{n+1} = t_n + \Delta t_{n+1}$; $\bar{\boldsymbol{\Sigma}}_0^{iter}(t_{n+1}) = \bar{\boldsymbol{\Sigma}}(t_n)$;
for $k = 0 : N_{iter}$ **do**
  $\delta \boldsymbol{E}_k = \boldsymbol{C}_0^{-1}(\boldsymbol{\Sigma}^{BC} - \bar{\boldsymbol{\Sigma}}_k^{iter})$;
  $\Delta \boldsymbol{E}_k = \delta \boldsymbol{E}_k + \Delta \boldsymbol{E}^{BC}$;
  $\boldsymbol{E}(t_{n+1}) = \boldsymbol{E}(t_n) + \Delta \boldsymbol{E}_k$;
  Call algorithm 1 to compute $\bar{\boldsymbol{\Sigma}}_{iter}^{k+1}(t_{n+1})$, $\boldsymbol{\sigma}^{k+1}(t_{n+1}, \boldsymbol{x}_p)$, $d^{k+1}(t_{n+1}, \boldsymbol{x}_p)$;
  if $\|\delta \boldsymbol{E}_k\| / \|\Delta \boldsymbol{E}_k\| < 10^{-4}$ **then**
    Calculate the macroscopic stress and phase field variable
    $\boldsymbol{\Sigma}(t_{n+1}) = \frac{1}{|\Omega|} \int_\Omega \boldsymbol{\sigma}(t_{n+1}, \boldsymbol{x}_p) dV$;
    $D(t_{n+1}) = \frac{1}{|\Omega|} \int_\Omega d(t_{n+1}, \boldsymbol{x}_p) dV$;
    Exit;
  else
    $k = k + 1$
  end
end

5. Numerical performances for heterogeneous materials

With the proposed PFFT method in hand, a number of numerical examples are considered here to validate its ability and accuracy for the description of cracking behavior in

heterogeneous geomaterials. For each example, we will select a specific micro-structure or representative volume element(RVE). Further, all examples are studied in 3D configuration.

5.1. Example 1: Tension test of a homogeneous unit cell

We firstly begin with a 3D homogeneous material imposing a macroscopic tensile strain $\boldsymbol{E} = 0.1\boldsymbol{e}_3 \otimes \boldsymbol{e}_3$. The size of the unit cell is $1 \times 1 \times 1$ mm as presented in Fig.2(a). For the case of homogeneous materials, here we first adopted the classical damage degradation function $g_1(d)$ to compare with the analytical results given by Molnár and Gravouil (2017) and Hirshikesh et al. (2019) with E_s=210GPa, $\nu_s = 0.3$, $g_c = 5{\times}10^{-3}$kN/mm, l_c=0.1mm. In addition, the viscous effect is not considered here. The loading history is divided into 1000 steps with a constant strain increment $\Delta\boldsymbol{E} = 1.0 \times 10^{-4}\boldsymbol{e}_3 \otimes \boldsymbol{e}_3$.

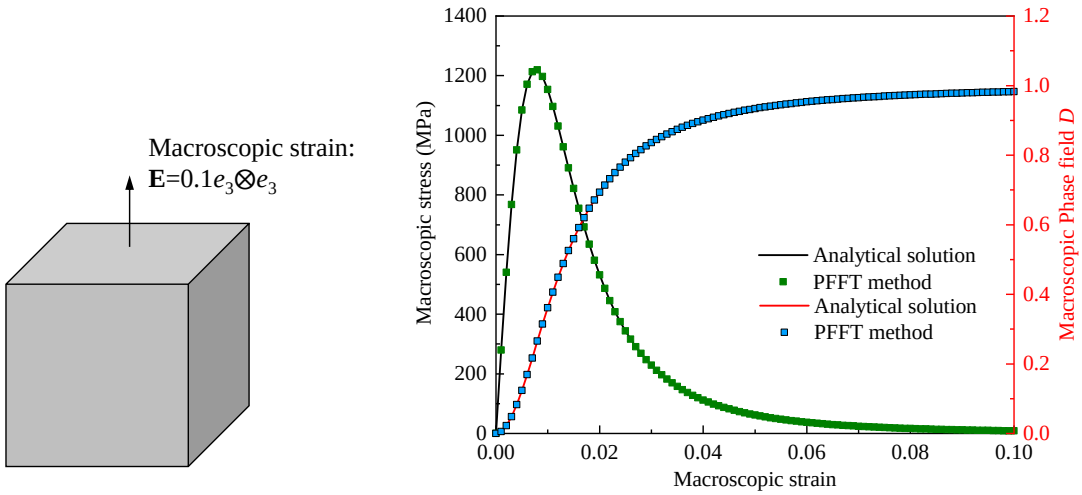

(a) 3D homogeneous unit cell

(b) Stress-strain curves and evolution of macroscopic damage variable D

Figure 2: Studied homogeneous unit cell and comparisons of stress-strain curves and macroscopic damage evolution between analytical solution and numerical results by proposed method

Figure 2(b) shows the comparisons of macroscopic stress-strain relation and damage evolution between the analytical solution and the proposed PFFT method. Obviously, these two solutions well recover each other as illustrated in this figure. This shows that the proposed FFT-based phase field method can well describe the damage process in homogeneous materials. In addition, in Figure 3 and 4, one presents the results predicted by the using new degradation function with different values of A and B. However, the analytical solution with the new degradation function is not available. It is clear that the post-peak responses

strongly depend on the values of A and B. With a bigger A or a smaller B, a lower peak failure strength is obtained. On the other hand, the material becomes more ductile with the increase of B.

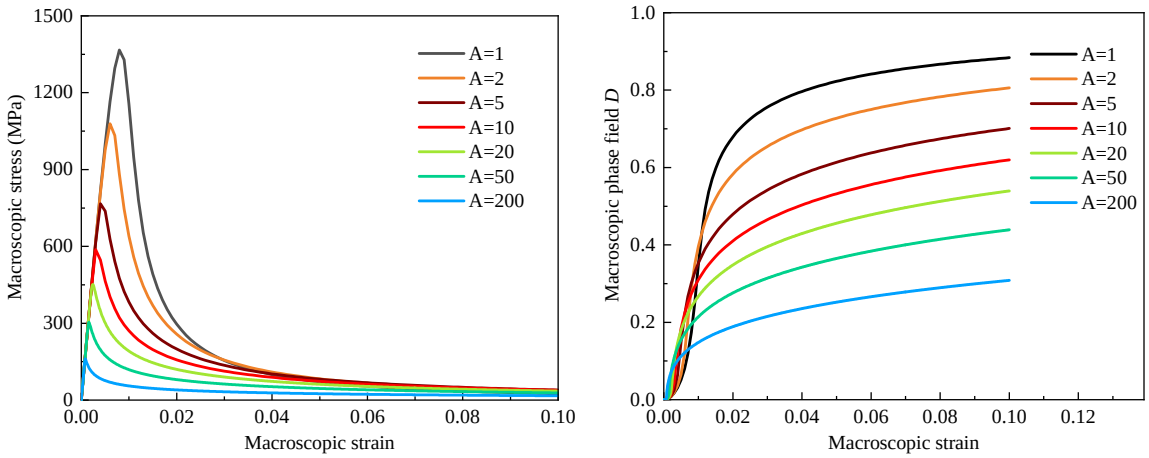

(a) Evolution of effective stress-strain relations (b) Evolution of macroscopic damage variable D

Figure 3: Evolution of macroscopic responses with different values of A when $B = 0.5$

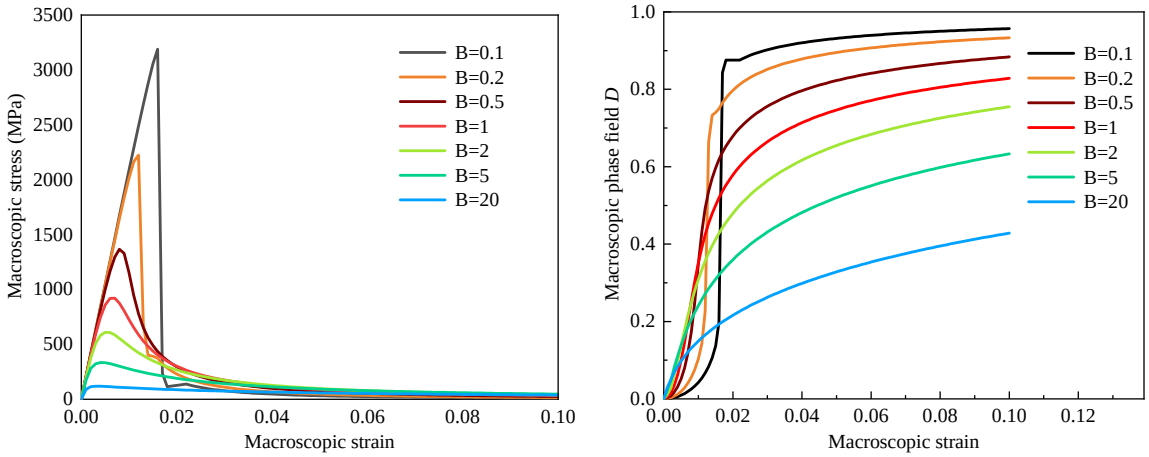

(a) Evolution of effective stress-strain relations (b) Evolution of macroscopic damage variable D

Figure 4: Evolution of macroscopic responses with different values of B when $A = 1$

5.2. Example 2: Uniaxial tension test of a single notched cubic cell

In order to verify the accuracy of this PFFT method to describe the crack propagation, a single notched cubic microstructure is considered with $64 \times 64 \times 64$ voxels. The size of the unit cell is $1 \times 1 \times 1$ mm. The initial crack geometry is depicted in Figure 5 and has

a thickness of one voxel size. The input parameters are taken as the ones in Miehe et al. (2010a): E_s =210GPa, ν_s = 0.3, η = 0Pa·s, l_c=0.0075mm, and g_c = 2.7×10^{-3}kN/mm. The cracked notch is regarded as void with zero stiffness. Differently with the classical 2D case considered in the previous studies (Miehe et al., 2010b,a; Kiendl et al., 2016), the periodic boundary conditions are prescribed here and consistent with the assumption of FFT-based method. The uniaxial tension test with a macroscopic tensile strain is applied within 200 steps, and the strain increment for each step is taken as $\Delta \boldsymbol{E} = 5.0 \times 10^{-5} \boldsymbol{e}_3 \otimes \boldsymbol{e}_3$.

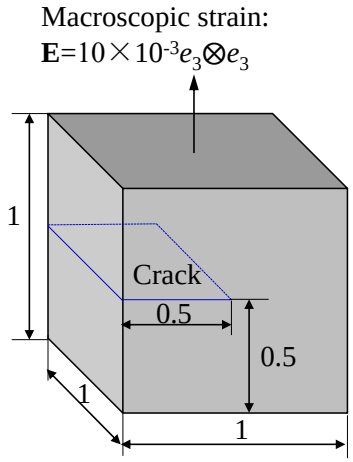

Figure 5: Single notched unit cell subjected to uniaxial tensile strain

The problem is firstly solved by using the classical degradation function $g_1(d)$. Figure 7 presents the simulated macroscopic stress and strain relation by the proposed PFFT method, and compared with that given in (Miehe et al., 2010a) by using direct FEM simulation and that in Chen et al. (2019) by adopting an explicit Fourier-based phase field method (denoted as Ex-PFFT method). It is found that a rapid convergence with very low residual stress is observed with the PFFT method. Further, the results provided by the proposed method are very close to the reference FEM solution, while the explicit Ex-PFFT method shows large scatters. In Figure 6, the results on the crack growth pattern during the loading history are visualized by red color. The three crack patterns correspond to the three selected loading step a, b and c as shown in Figure 7. It is found that evolution of crack pattern is quite different with that reported by Miehe et al. (2010a); Molnár and Gravouil (2017) and Martínez-Pañeda et al. (2018). Due to the periodic boundary conditions used here, two new micro-cracks start to initiate and gradually propagate at the two ends of the notch, finally join each to other. This indicates the crack phase field is accurately calculated by the implicit iterate process.

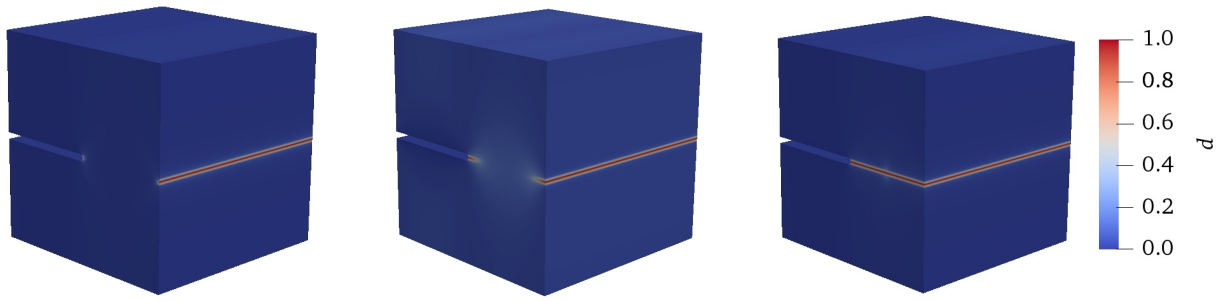

(a) Pattern a (b) Pattern b (c) Pattern c

Figure 6: Crack growth patterns visualized by red color of a single notched unit cell under uniaxial tensile test

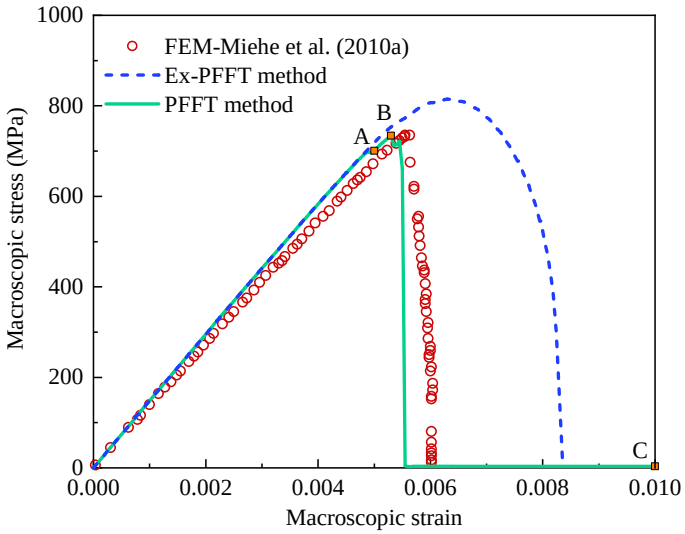

Figure 7: Macroscopic stress strain curves of a single notched unit cell under uniaxial tension and comparison with results with different methods

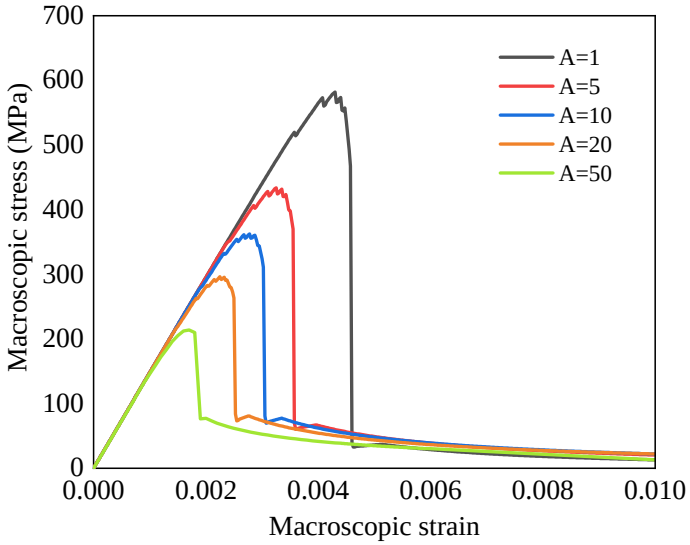

Figure 8: Effective behaviors for different selection of A when B=1 for unit cell with 64^3 voxel resolutions

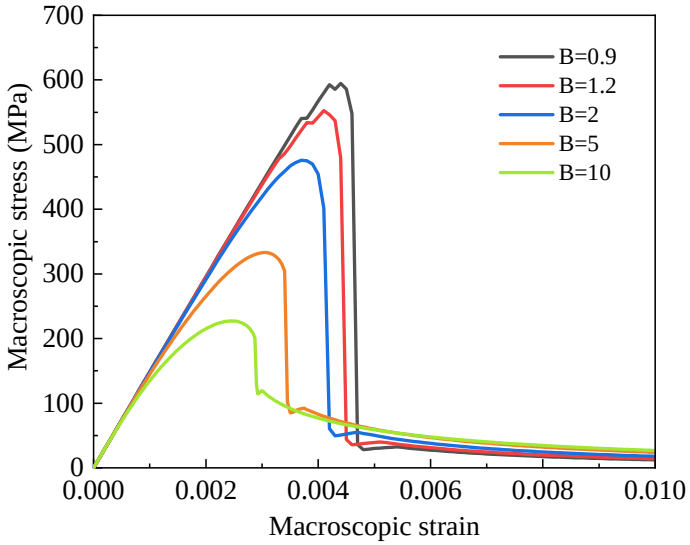

Figure 9: Effective behaviors for different selection of B when A=1 for unit cell with 64^3 voxel resolutions

In addition, calculations with the new degradation function are also performed. In Figure 8 and 9, overall axial stress-strain relations are revealed for different choices of A and B. The peak strength decreases when the value of A or B increases. The failure mode turns from brittle to ductile when the value of B increases. In addition, both the pre-peak nonlinear

deformation and the residual stage after post failure can be well captured. The selection of A and B should be determined by the mechanical properties of material though experimental studies.

To further clarify the convergence of the new degradation function, the solver with classical quadratic function is also compared. Since the mixed boundary conditions is applied on the unit cell, both the Newton iteration and FFT iteration are considered. Then three combinations with different values of A and B for the proposed degradation function are selected here as comparisons. Figure 10 and Figure 11 respectively present a comparison of Newton iterations and FFT iterations consumed at each loading step for different selection of degradations. As shown in Figure 10 and Figure 11, the solver with quadratic function needs more Newton and FFT iteration numbers to converge than the proposed one, especially after the onset of failure and during the residual stress stage. The maximum consumed Newton and FFT iteration numbers appears at the loading step when the stress drop occurs after onset of failure. The total consumed iteration numbers have listed in Table 1 for each case. It is clear that the proposed solver with the new degradation function is much more efficient than the one with classical degradation function.

Table 1: Newton iteration and FFT iteration numbers consumed by using different degradation function

Degradation function	Maximum iteration numbers after onset of failure		Total iteration numbers	
	Newton	FFT	Newton	FFT
Quadratic function	192	3541	11911	39718
Proposed one with A=1, B=1	232	1226	9063	26227
Proposed one with A=5, B=1	231	1060	9533	26492
Proposed one with A=1, B=2	212	1541	6588	23883

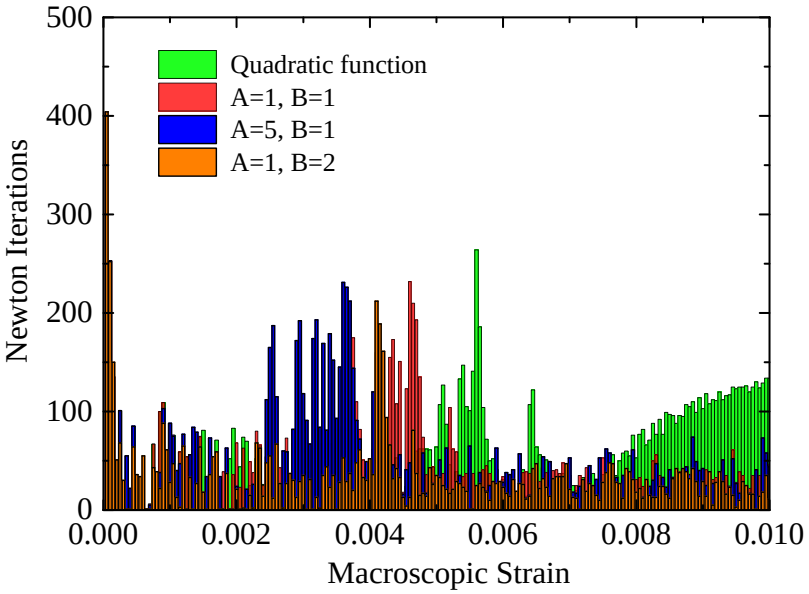

Figure 10: Comparisons of Newton iteration numbers consumed between the solver with quadratic degradation function and the proposed one at each loading step

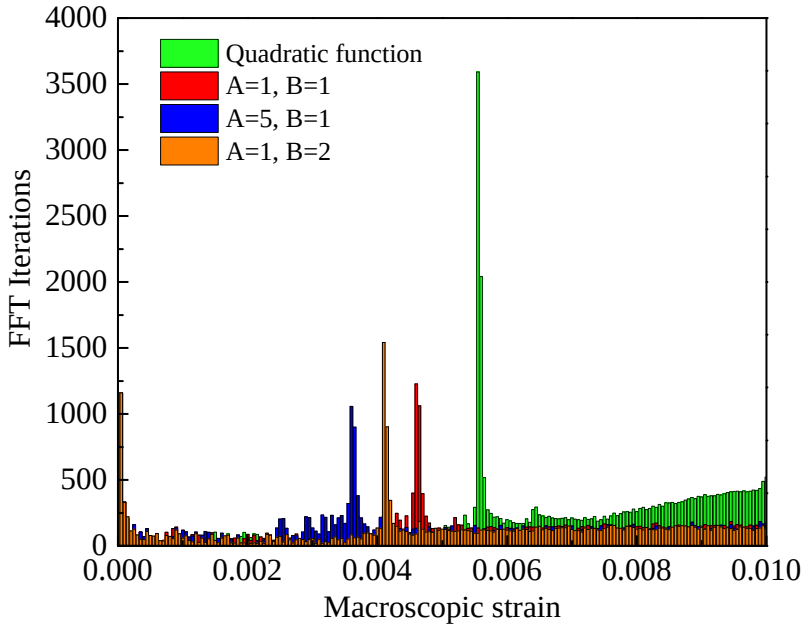

Figure 11: Comparisons of FFT iteration numbers consumed between the solver with quadratic degradation function and the proposed one at each loading step

5.3. Example 3: Tension tests of a microstructure with one void or inclusion

Both porous materials and inclusion-reinforced material are investigated in this section to show the efficiency of the proposed PFFT model for describing the damage and cracking behavior in heterogeneous materials. All the cubic unit cells studied here have a size of $1 \times 1 \times 1$ mm.

5.3.1. Case of porous materials

As illustrated in Figure 12, the microstructure with a spherical void located at the center is chosen to represent the periodic porous materials. The porosity of the unit cell is 5%. The resolution used for FFT method is $128 \times 128 \times 128$ voxels. The material properties of the solid matrix are: E_s=100GPa, $\nu_s = 0.15$, g_c=2.0×10^{-3}kN/mm, $A = 2$ and $B = 5$, and the length scale is l_c=0.015mm. The computation is performed under uniaxial tension condition within a strain increment of $\Delta \boldsymbol{E} = 2.5 \times 10^{-5} \boldsymbol{e}_3 \otimes \boldsymbol{e}_3$ within a time step $\Delta t = 25s$. For heterogeneous rock-like materials, it has been realized that due to heterogeneity, rock failure is not instantaneous but progressive. The viscous regularization with the parameter η can delay the aggressive crack growth in the post critical regime. The effect of viscous parameter η on the effective behavior of heterogeneous material is shown in Figure 13. It is found that the macroscopic behavior of unit cell is significantly influenced by the viscosity parameter. The macroscopic stress-stain response shows a sharp decline for the case $\eta = 0$ whereas the viscous regularization model smoothes out the brutal crack propagation in the post critical regime. This has also been clarified in Miehe et al. (2010a) and Chen et al. (2019). The cracking patterns at four different time steps indicated in Figure 13 for the case of $\eta = 10^5$Pa·s are shown in Figure 14. It is seen that cracks initiate on the void surface and propagate towards the solid matrix. Therefore, the following numerical tests will use the viscous regularization to present the progressive cracking process in detail. It is worth to note that the value of η should be selected carefully, since a too high value of η can lead to unrealistic prediction of the critical stress, as indicated by Chen et al. (2019).

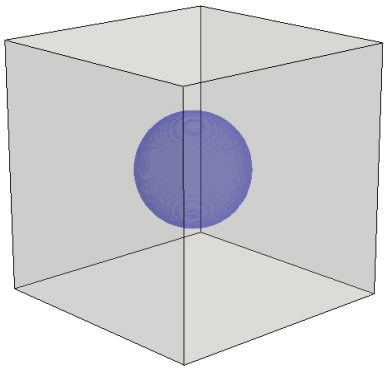

Figure 12: Unit cell containing one centered spherical void with porosity $f = 5\%$

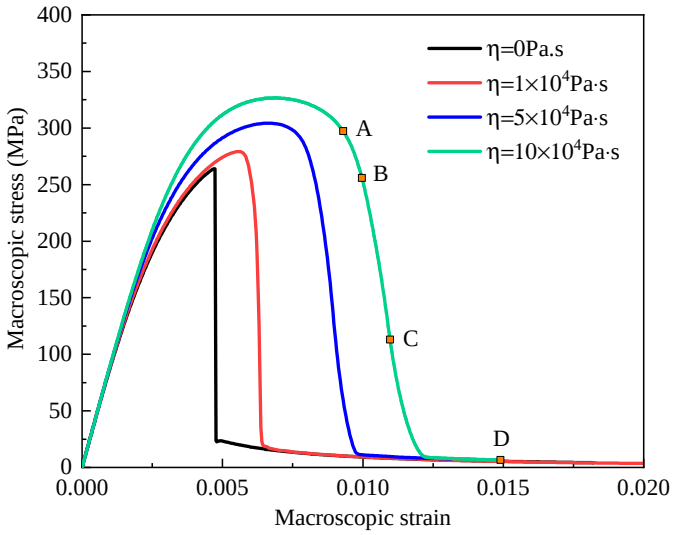

Figure 13: Macroscopic axial stress-strain curves for unit cell containing one centered spherical void with different values of η

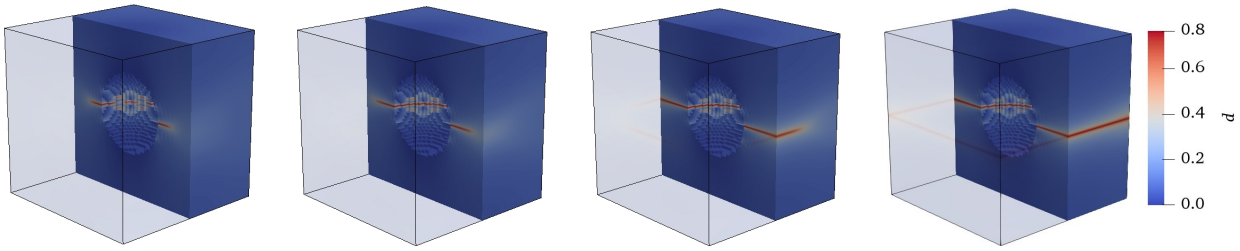

(a) Step A (b) Step B (c) Step C (d) Step D

Figure 14: Phase field patterns of the unit cell under uniaxial tension test at different time steps with $\eta = 10^5$ Pa·s

It is known that the void shape has important effects on the local and overall responses of porous materials. To illustrate this point, we particularly conducted several simulations on the unit cell respectively containing an oblate or a prolate void, with a porosity of 5%. The aspect ratio of the oblate void is 2 while that of the prolate one is 0.5. Figure 15 and 16 respectively depict the crack patterns for spheroidal voids, each with three different orientations, namely $\omega = 0°$, $45°$, $90°$. The crack label is as same as the one in Figure 14. Here we define ω as the orientation angle between the loading direction e_3 and the minor (symmetric) axis for the oblate void, or the major (symmetric) axis for the prolate one. As shown in Figure 15 and 16, the main crack grows around the middle surface of void for the orientations $\omega = 0°$ and $\omega = 90°$. However, for the case of $\omega = 45°$, the main crack firstly initiates from the surface of void and then propagates with a small inclination angle with the loading direction. In addition, a non-penetrating crack is also captured for this void orientation. In Figure 17, the corresponding macroscopic stress strain curves are given. The influences of the void shape and orientation on the overall responses are clearly illustrated.

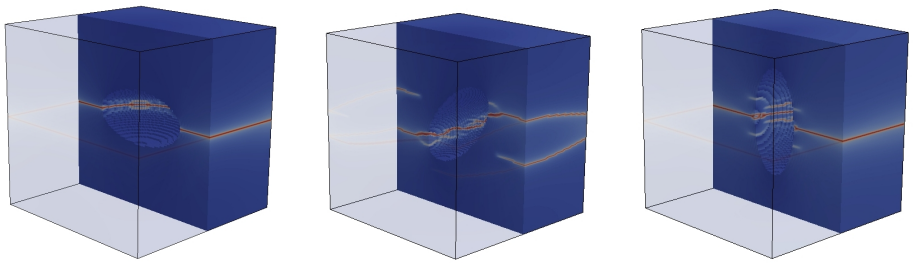

(a) $\omega = 0°$ (b) $\omega = 45°$ (c) $\omega = 90°$

Figure 15: Crack patterns of the unit cell with oblate void of different orientations under uniaxial tension test: $\eta = 10^4$Pa·s

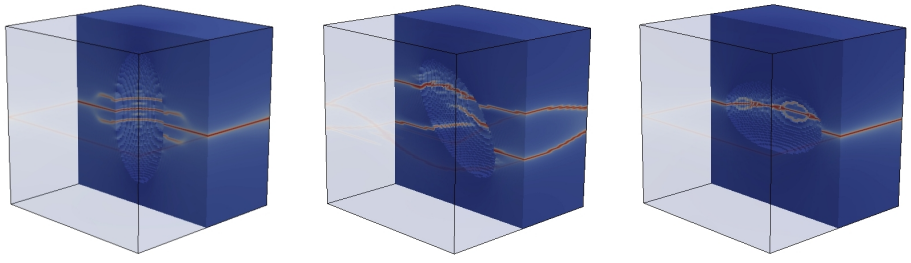

(a) $\omega = 0°$ (b) $\omega = 45°$ (c) $\omega = 90°$

Figure 16: Crack patterns of the unit cell with prolate void of different orientations under uniaxial tension test: $\eta = 10^4$Pa·s

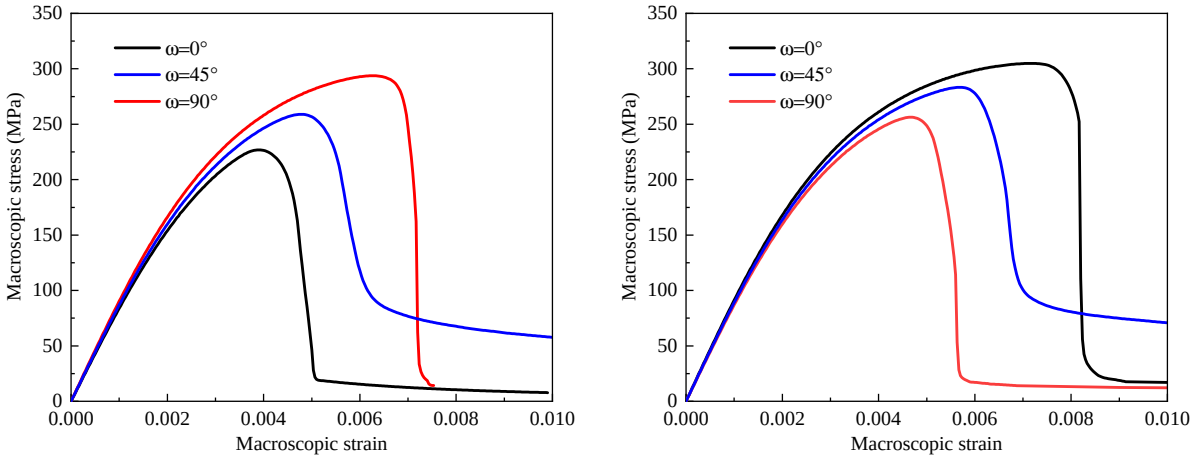

(a) Oblate void (b) Prolate void

Figure 17: Macroscopic axial stress-strain curves for different void orientations under uniaxial tension test: $\eta = 10^4$Pa·s

5.3.2. Case of inclusion-reinforced materials

For inclusion-reinforced materials, calculations are realised on the unit cell with a centered rigid spherical inclusion under uniaxial tension. The representative unit cell is displayed in Figure 18. The material parameters of the solid matrix are E_s=20GPa, $\nu_s = 0.15$, l_c=0.015mm, g_c=2.0×10^{-3}kN/mm, $\eta = 10^4$Pa·s, $A = 2$ and $B = 5$. For the elastic rigid inclusion, the elastic parameters are $E_i = 200$ GPa and $\nu_i = 0.15$. The macroscopic strain in the direction $\boldsymbol{e}_3$ is prescribed in 600 steps with the increment of $\Delta \boldsymbol{E} = 3.33 \times 10^{-5} \boldsymbol{e}_3 \otimes \boldsymbol{e}_3$ for each step. The total loading process is set to $T = 1 \times 10^4$s. In Fig.19, one presents the crack patterns at four selected time steps. Differently with the case of porous materials shown in Figure 14, the initiation of two symmetric micro-cracks is captured which begin at the top and bottom interfaces of the inclusion, and then propagate across the unit cell.

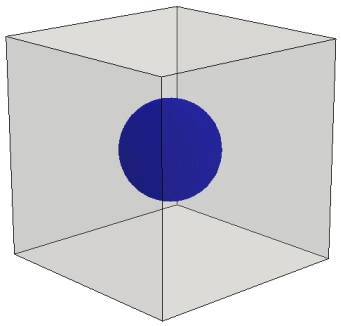

Figure 18: Studied inclusion-reinforced materials having one centered inclusion ($\rho = 5\%$)

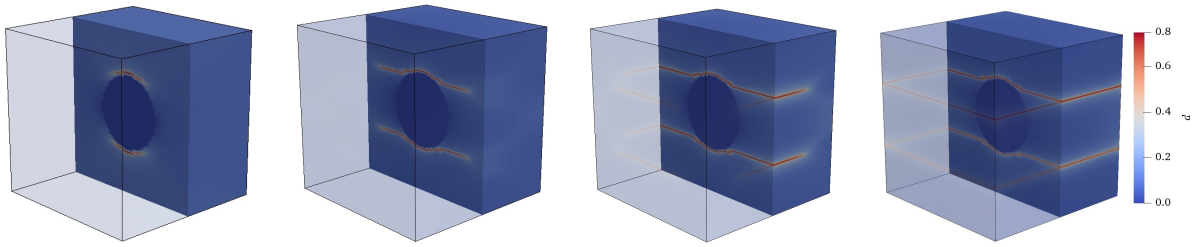

(a) Pattern at step 1 (b) Pattern at step 2 (c) Pattern at step 3 (d) Pattern at step 4

Figure 19: Crack patterns of the unit cell under uniaxial tensile test: $\eta = 10^4 Pa.s$

The effects of orientations for different inclusion shape are also investigated. In Figure 20 and 21, one presents the crack patterns in the unit cells containing an oblate or a prolate inclusion of three different orientations. It is observed that in all cases, two main cracks initiate from and propagate along the inclusion-matrix interface before penetrating into the matrix. The crack propagation direction is related to the inclusion geometry and orientation. The corresponding evolution of macroscopic stress-strain is given in Figure 22. The peak strength is strongly determined by the inclusion geometry and orientation. For the case of oblate inclusion, the maximum peak strength is obtained for $\omega = 0°$ while it is found for $\omega = 90°$ for the prolate one. The provided results have clearly discrepancy with that found in the unit cells with an oblate or prolate void.

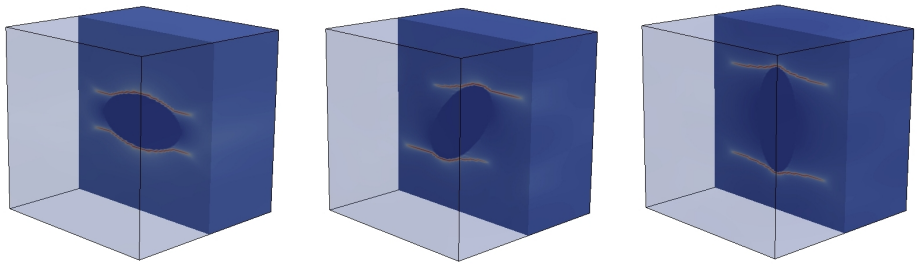

(a) $\omega = 0°$ (b) $\omega = 45°$ (c) $\omega = 90°$

Figure 20: Crack propagation patterns of the unit cell containing an oblate inclusion of three different orientations under uniaxial tension test

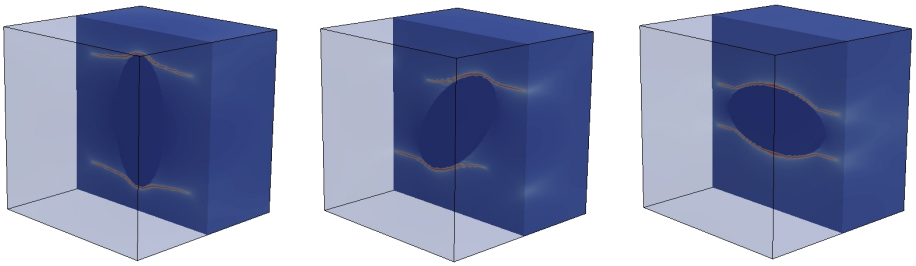

(a) $\omega = 0°$ (b) $\omega = 45°$ (c) $\omega = 90°$

Figure 21: Crack propagation patterns of the unit cell containing a prolate inclusion of three different orientations under uniaxial tension test

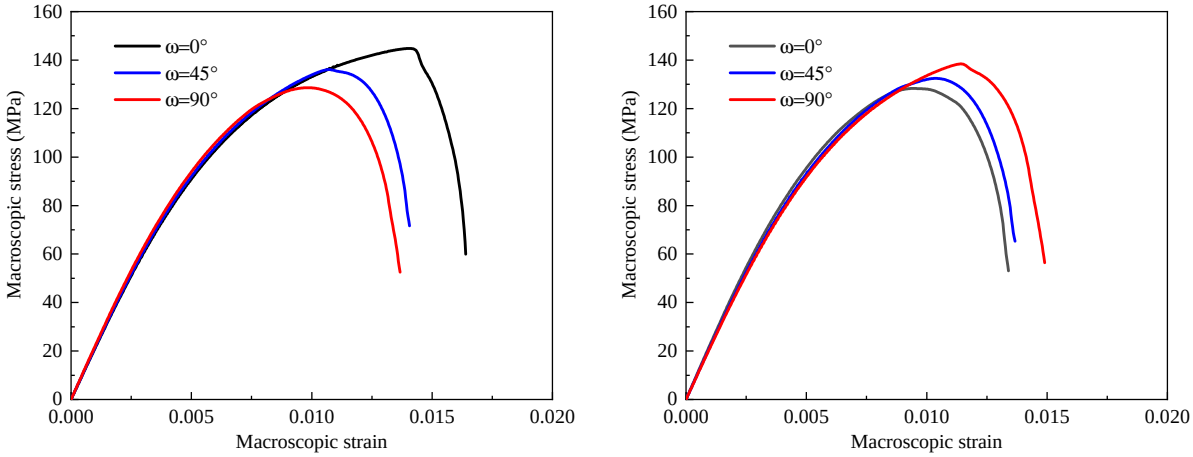

(a) Oblate inclusion (b) Prolate inclusion

Figure 22: Macroscopic axial stress-strain curves of the unit cells with different inclusion orientations under uniaxial tension test

5.4. Example 4: Porous material with randomly arranged voids or inclusions under different loading paths

In this subsection, particular attentions will be put on the macroscopic mechanical behavior of the unit cells containing randomly distributed voids or inclusions. This kind of micro-structures are assumed to be representative of some rock-like materials.

5.4.1. Uniaxial tension test

The uniaxial tension test is first considered. Three different micro-structures are selected: unit cell with randomly distributed pores (porosity $f = 20\%$), unit cell with randomly distributed inclusions (inclusion volume fraction $\rho = 20\%$) and unit cell with both randomly

embedded pores and inclusions at same scale (porosity $f = 10\%$, inclusion volume fraction $\rho = 10\%$). As an example, the unit cell with random pores is shown in Fig.23. Each cubic unit cell is discretized with $128 \times 128 \times 128$ voxels. As in the section 5.3, the same input material properties chosen.

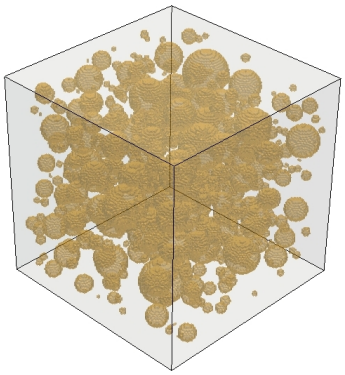

Figure 23: Typical unit cell of porous material

Figure 24 compares the obtained macroscopic behaviors of these three unit cells. There is a significant difference between three micro-structures. Logically, the peak strength is maximum for the inclusion-reinforced material and minimum for the porous material. The material with pores and inclusion at the same scale is between these two extreme cases. At the same time, it seems that the porous unit cell exhibits a less brittle cracking mode than the inclusion-reinforced one. Figure 25 show the cracking paths of these three unit cells at the end of loading. All the three unit cells are dominated by the tensile cracking but the spatial distribution of cracks appears clearly different.

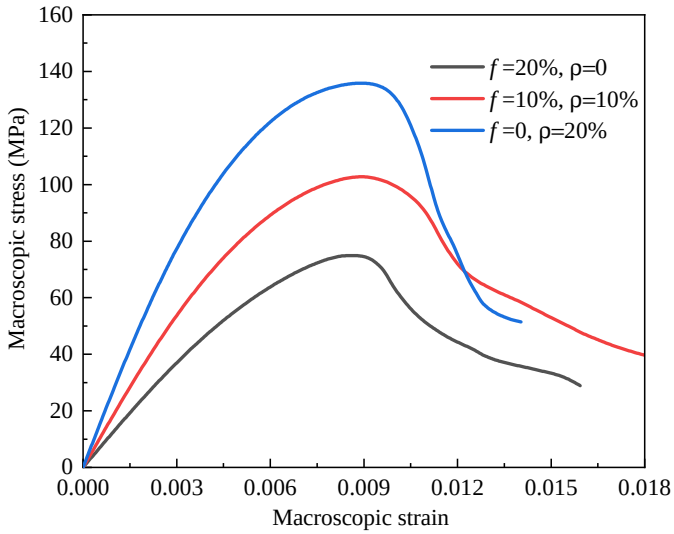

Figure 24: Macroscopic stress strain relations for three different unit cells

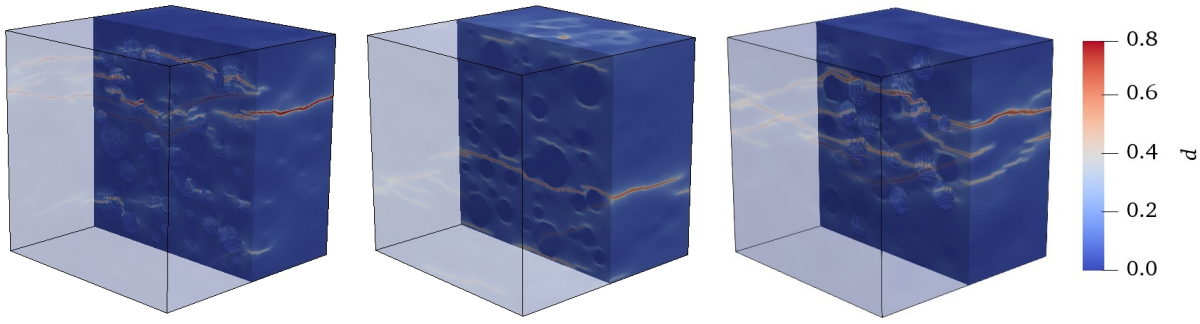

(a) $f = 20\%, \rho = 0\%$ (b) $f = 0\%, \rho = 20\%$ (c) $f = 10\%, \rho = 10\%$

Figure 25: Cracking patterns of three different unit cells with randomly distributed pores or inclusions in uniaxial tension test

5.4.2. Triaxial extension test on porous materials

In this case, the unit cell with randomly distributed pores is firstly subjected to a hydrostatic confining stress ($\Sigma^0_{11} = \Sigma^0_{22} = \Sigma^0_{33}$). Then, a macroscopic tension strain is prescribed along the axis e_3 while the confining stress in the other two directions is kept constant. Three different values of confining stress are used such as -5MPa, -10MPa and -15MPa. The prescribed strain increment is $\Delta E_{33} = 3.33 \times 10^{-5}$. The predicted cracking patterns are reported in Figure 26. It is found that the main crack for each case is almost perpendicular to the strain loading direction. In addition, it seems that the confining stress has an insensitivity to the cracking pattern. Similar results have been reported in Liu et al. (2019) for triaxial

extension tests performed on sandstone. However, Figure 27(a) reveals an increase of peak deviatoric strength with the increasing confining stress . For instance, the corresponding peak strengths are 74.9MPa, 74.5MPa, 74.1MPa and 73.7MPa when the confining stress increases from 0MPa to -15MPa. It implies that the compressive confining stress in the directions e_1 and e_2 can affect the tensile cracking process in the direction e_3.

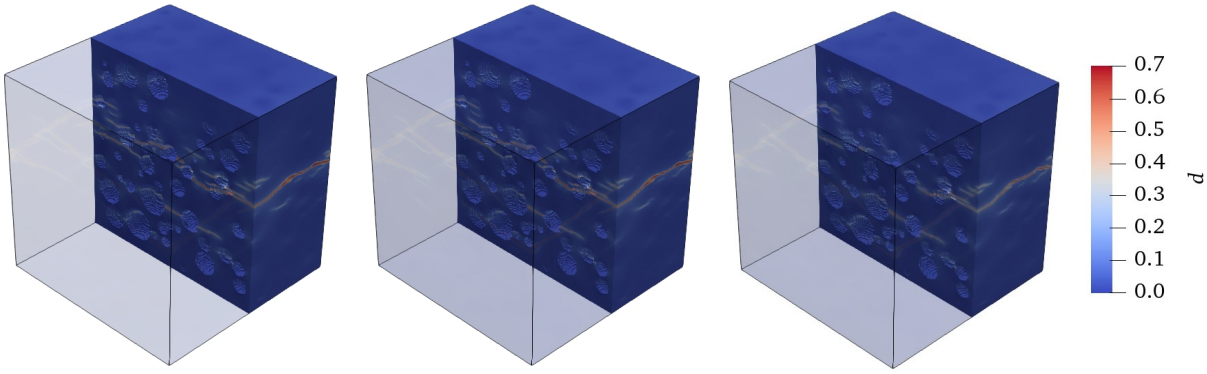

(a) Σ_{11}=-5MPa (b) Σ_{11}=-10MPa (c) Σ_{11}=-15MPa

Figure 26: Cracking patterns of the unit cell with randomly distributed pores in triaxial extension test with different confining stress (f = 20%)

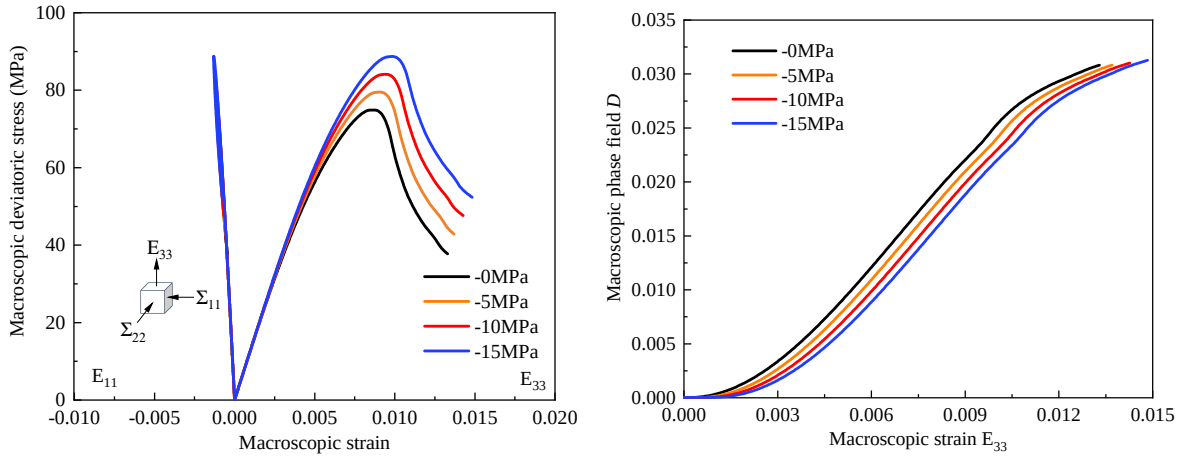

(a) Macroscopic stress-strain curves (b) Macroscopic phase field evolution

Figure 27: Macroscopic stress strain curves and evolution of damage variable D in triaxial extension test (f = 20%)

5.4.3. Triaxial compression test on porous materials

Finally, the commonly used conventional triaxial compression test for rock-like materials is studied. The unit cell is the same as that in Figure 26. Differently with the triaxial exten-

sion test presented above, after the loading of confining stress, a compressive macroscopic strain is prescribed alone the e_3 direction. The obtained macroscopic mechanical behavior is shown in Figure 28(a), including those obtained in the uniaxial compression test. As for the triaxial extension test, the peak deviatoric stress increases with the increasing confining stress. Further, the high confining stress attenuates and delays the evolution of the macroscopic damage variable as illustrated in Figure 28(b). This reveals that the under triaxial compression condition, shear cracking is generally the main process and the confining stress has restricting effect on this process due to the compressive normal stress applied to crack surfaces. In Figure 29, one finds the cracking patterns at the end of loading process. Complex crack networks are observed in the unit cells under the triaxial compressive stress state. This is clearly different from the triaxial extensile test. Even if the phase field evolution is driven by the elastic free energy associated with the tensile strains only, owing to the presence of pores, cracks can initiate and propagate in different orientations. However, due to this simple damage evolution law, the cracking patterns under triaxial compression are quite similar to those in uniaxial compression. The effect of confining stress on cracking pattern is no correctly described by the current damage evolution law. This issue will be considered in a future study by developing suitable damage evolution laws involving shear strains.

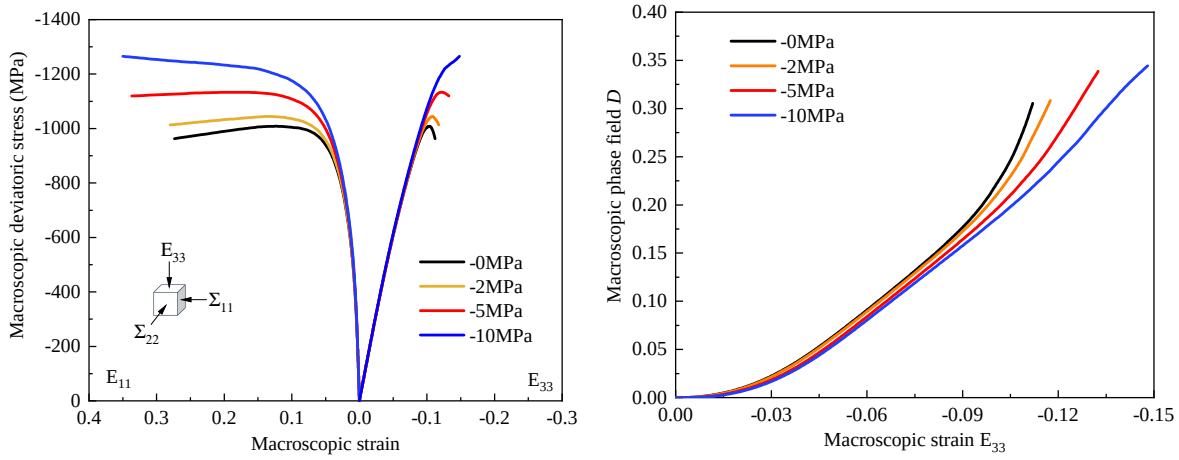

(a) Macroscopic stress-strain curves

(b) Macroscopic phase field evolution

Figure 28: Macroscopic stress strain curves and evolution of macroscopic damage variable D with different confining stresses ($f = 20\%$)

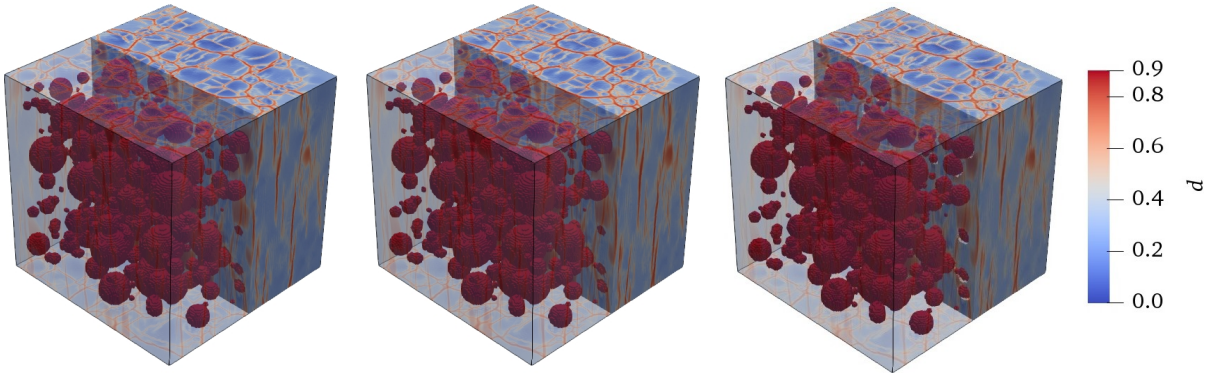

(a) Σ_{11}=-0MPa (b) Σ_{11}=-5MPa (c) Σ_{11}=-10MPa

Figure 29: Cracking patterns of the unit cell with randomly distributed pores in triaxial compression tests with different confining stresses (f = 20%)

6. Experimental validation

In this section, an experimental validation of the proposed PFFT method for heterogeneous material will be provided. Two direct tensile experiments of porous rock materials from Hashiba and Fukui (2015) will be simulated to show the effectiveness of this method: the uniaxial tension tests of the dry Komatsu andesite (KA) and Sanjome andesite(SA). The porosities of these two samples are 16.1% and 13.3%, respectively. For simplicity, it is assumed that the porous rock is composed of solid matrix and voids. The cubic RVE random distributed spherical voids is selected here for the simulations. The porosity of the RVE is configured as same as the real rock specimen in Hashiba and Fukui (2015). The material parameters of the two specimens are listed in Table 2.

Table 2: Material parameters of studied porous rock samples

Materials	Solid matrix	void
KA	E_s = 19.4GPa, ν_s = 0.14	E_i = 0GPa, ν_i = 0, f = 16.1%
	g_c = 1.9N/m, l_c = 0.007mm, η = 0 Pa·s	
	A = 2, B = 2.8	
SA	E_s = 18.3GPa, ν_s = 0.14	E_i = 0GPa, ν_i = 0, f = 13.3%
	g_c = 2.1N/m, l_c = 0.01mm, η = 0 Pa·s	
	A = 2.5, B = 3.1	

Figure 30(a) and 30(b) present a comparison of macroscopic stress-strain curves between the simulated results by using the PFFT method (black solid line) and the experimental data (red square point). It is clear that the modeling results are consistent with the experimental data for both samples. Particularly, both the nonlinear pre-failure deformation and the residual stress stage during the post-peak failure are well captured by the proposed model. In addition, the corresponding failure modes of this two porous materials predicted by the proposed PFFT model are compared in Figure 30(c) and 30(d) with the experimental ones Hashiba and Fukui (2015). These two failure forms are quite similar. It can be observed that the specimens failed on a plane that was approximately perpendicular to the loading axis. These planes were located at weakest part of the specimens, where the tensile stress was supposed to be uniformly distributed. This is the typical tensile failure mode for brittle rock-like materials. Similar experimental results also can be found in Zhang et al. (2017) and Shang et al. (2016).

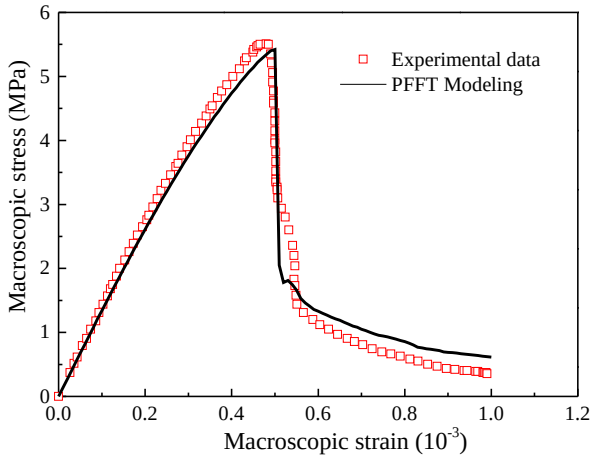

(a) Komatsu andesite (KA), f = 16.1%

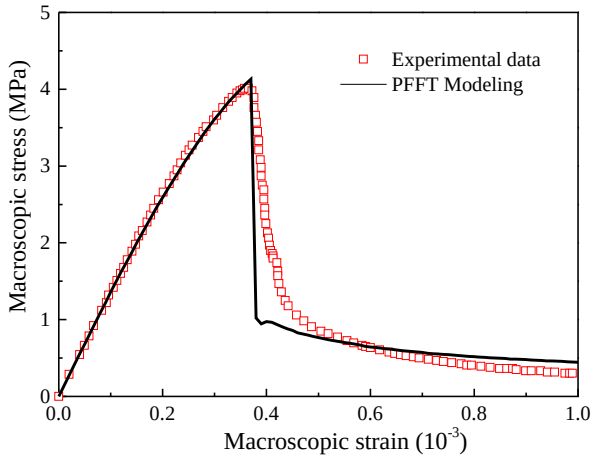

(b) Sanjome andesite (SA), f = 13.3%

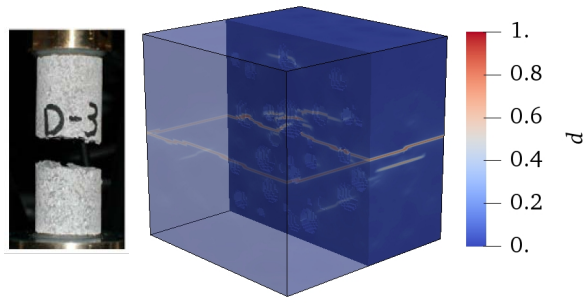

(c) Failure mode (KA)

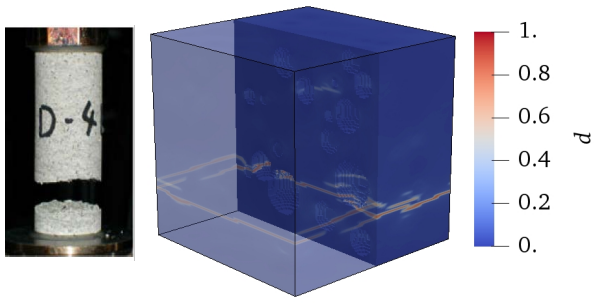

(d) Failure mode (SA)

Figure 30: Comparisons between the experimental data from Hashiba and Fukui (2015) and the PFFT modeling results under uniaxial tension test

7. Concluding remarks

In this work, a new numerical method was established for cracking behavior in rock-like heterogeneous materials by combining FFT-based homogenization procedure and phase-field method. In addition, a new decoupling strategy has also been problem for efficiently solving the stress-strain and crack phase field problems. This new algorithm provides an implicit solver of phase field and its accuracy has been well demonstrated by both analytical solutions and experimental validations. The developed method is efficient for three-dimensional modeling of damage evolution, nucleation and propagation of localized cracks by considering interactions with different kinds of heterogeneities. In addition, with the new introduced degradation function, the proposed PFFT method can describe a large range of cracking processes in rock-like materials. A series of numerical studies have been performed on heterogeneous materials under different loading paths. The obtained results have clearly shown that the macroscopic responses and cracking patterns of heterogeneous materials are highly affected by heterogeneity features such as volume fraction, shape, size, orientation, and spatial distribution.

Acknowledgements

This study was supported by the Programme B18019 of Discipline Expertise to Universities MOE & MST.

References

Ambati, M., Gerasimov, T., De Lorenzis, L., 2015. Phase-field modeling of ductile fracture. Computational Mechanics 55 (5), 1017–1040.

Bazant, Z. P., Pijaudier-Cabot, G., 1988. Nonlocal continuum damage, localization instability and convergence.

Borden, M. J., 2012. Isogeometric analysis of phase-field models for dynamic brittle and ductile fracture. Ph.D. thesis.

Borden, M. J., Hughes, T. J., Landis, C. M., Anvari, A., Lee, I. J., 2016. A phase-field formulation for fracture in ductile materials: Finite deformation balance law derivation, plastic degradation, and stress triaxiality effects. Computer Methods in Applied Mechanics and Engineering 312, 130–166.

Borden, M. J., Hughes, T. J., Landis, C. M., Verhoosel, C. V., 2014. A higher-order phase-field model for brittle fracture: Formulation and analysis within the isogeometric analysis framework. Computer Methods in Applied Mechanics and Engineering 273, 100–118.

Borden, M. J., Verhoosel, C. V., Scott, M. A., Hughes, T. J., Landis, C. M., 2012. A phase-field description of dynamic brittle fracture. Computer Methods in Applied Mechanics and Engineering 217-220, 77 – 95.

Bourdin, B., Francfort, G., Marigo, J.-J., 2000. Numerical experiments in revisited brittle fracture. Journal of the Mechanics and Physics of Solids 48 (4), 797 – 826.

Brisard, S., Dormieux, L., 2010. FFT-based methods for the mechanics of composites: a general variational framework. Computational Material Science 49,3, 663–671.

Broumand, P., Khoei, A., 2013. The extended finite element method for large deformation ductile fracture problems with a non-local damage-plasticity model. Engineering Fracture Mechanics 112, 97–125.

Cao, Y., Shen, W., Burlion, N., Shao, J., 2018a. Effects of inclusions and pores on plastic and viscoplastic deformation of rock-like materials. International Journal of Plasticity 108, 107 – 124.

Cao, Y., Shen, W., Shao, J., Burlion, N., 2018b. Influences of micro-pores and meso-pores on elastic and plastic properties of porous materials. European Journal of Mechanics - A/Solids 72, 407 – 423.

Chen, Y., Vasiukov, D., Gélébart, L., Park, C. H., 2019. A fft solver for variational phase-field modeling of brittle fracture. Computer Methods in Applied Mechanics and Engineering 349, 167 – 190.

Conte, S., De Boor, C., 2018. Elementary Numerical Analysis: An Algorithmic Approach. Classics in Applied Mathematics. Society for Industrial and Applied Mathematics (SIAM, 3600 Market Street, Floor 6, Philadelphia, PA 19104).

Dormieux, L., Kondo, D., 2016. Micromechanics of fracture and damage. John Wiley & Sons.

Duddu, R., Waisman, H., 2013. A nonlocal continuum damage mechanics approach to simulation of creep fracture in ice sheets. Computational Mechanics 51 (6), 961–974.

Eyre, D. J., Milton, G. W., 1999. A fast numerical scheme for computing the response of composites using grid refinement. The European Physical Journal Applied Physics 6, 41–47.

Feyel, F., 2003. A multilevel finite element method (fe2) to describe the response of highly non-linear structures using generalized continua. Computer Methods in Applied Mechanics and Engineering 192 (28), 3233 – 3244.

Fish, J., Yu, Q., Shek, K., 1999. Computational damage mechanics for composite materials based on mathematical homogenization. International journal for numerical methods in engineering 45 (11), 1657–1679.

Francfort, G., Marigo, J.-J., 1998. Revisiting brittle fracture as an energy minimization problem. Journal of the Mechanics and Physics of Solids 46 (8), 1319 – 1342.

Geers, M. G., Kouznetsova, V. G., Brekelmans, W., 2010. Multi-scale computational homogenization: Trends and challenges. Journal of computational and applied mathematics 234 (7), 2175–2182.

Gerasimov, T., Lorenzis, L. D., 2016. A line search assisted monolithic approach for phase-field computing of brittle fracture. Computer Methods in Applied Mechanics and Engineering 312, 276 – 303, phase Field Approaches to Fracture.

Gerasimov, T., Lorenzis, L. D., 2019. On penalization in variational phase-field models of brittle fracture. Computer Methods in Applied Mechanics and Engineering 354, 990 – 1026.

Hashiba, K., Fukui, K., 2015. Effect of water on the deformation and failure of rock in uniaxial tension. Rock Mechanics and Rock Engineering 48 (5), 1751–1761.

Hirshikesh, Natarajan, S., Annabattula, R. K., 2019. A fenics implementation of the phase field method for quasi-static brittle fracture. Frontiers of Structural and Civil Engineering 13, 380–396.

Kabel, M., Böhlke, T., Schneider, M., Dec 2014. Efficient fixed point and newton–krylov solvers for fft-based homogenization of elasticity at large deformations. Computational Mechanics 54 (6), 1497–1514.

Kiendl, J., Ambati, M., De Lorenzis, L., Gomez, H., Reali, A., 2016. Phase-field description of brittle fracture in plates and shells. Computer Methods in Applied Mechanics and Engineering 312, 374–394.

Kienle, D., Aldakheel, F., Keip, M.-A., 2019. A finite-strain phase-field approach to ductile failure of frictional materials. International Journal of Solids and Structures 172-173, 147 – 162.

Kuhn, C., Schlüter, A., Müller, R., 2015. On degradation functions in phase field fracture models. Compu-

tational Materials Science 108, 374–384.

Leclerc, J., Wu, L., Nguyen, V. D., Noels, L., 2018. A damage to crack transition model accounting for stress triaxiality formulated in a hybrid nonlocal implicit discontinuous galerkin-cohesive band model framework. International Journal for Numerical Methods in Engineering 113 (3), 374–410.

Li, M., Cao, Y., Shen, W., Shao, J., 2018. A damage model of mechanical behavior of porous materials: Application to sandstone. International Journal of Damage Mechanics 27 (9), 1325–1351.

Li, X., Chen, J., 2017. An extended cohesive damage model for simulating arbitrary damage propagation in engineering materials. Computer Methods in Applied Mechanics and Engineering 315, 744–759.

Liu, Z., Zhou, H., Zhang, W., Xie, S., Shao, J., 2019. A new experimental method for tensile property study of quartz sandstone under confining pressure. International Journal of Rock Mechanics and Mining Sciences 123, 104091.

Londono, J. G., Berger-Vergiat, L., Waisman, H., 2017. An equivalent stress-gradient regularization model for coupled damage-viscoelasticity. Computer Methods in Applied Mechanics and Engineering 322, 137–166.

Lu, G., Chen, J., 2020. A new nonlocal macro-meso-scale consistent damage model for crack modeling of quasi-brittle materials. Computer Methods in Applied Mechanics and Engineering 362, 112802.

Martin, C., Chandler, N., 1994. The progressive fracture of lac du bonnet granite. In: International journal of rock mechanics and mining sciences & geomechanics abstracts. Vol. 31. Elsevier, pp. 643–659.

Martínez-Pañeda, E., Golahmar, A., Niordson, C. F., 2018. A phase field formulation for hydrogen assisted cracking. Computer Methods in Applied Mechanics and Engineering 342, 742–761.

Meng, Q., Wang, H., Xu, W., Cai, M., Xu, J., Zhang, Q., 2019a. Multiscale strength reduction method for heterogeneous slope using hierarchical fem/dem modeling. Computers and Geotechnics 115, 103164.

Meng, Q.-X., Wang, H.-L., Xu, W.-Y., Chen, Y.-L., 2019b. Numerical homogenization study on the effects of columnar jointed structure on the mechanical properties of rock mass. International Journal of Rock Mechanics and Mining Sciences 124, 104127.

Michel, J. C., Moulinec, H., Suquet, P., 2001. A computational scheme for linear and non-linear composites with arbitrary phase contrast. International Journal for Numerical Methods in Engineering 52, 139–160.

Miehe, C., Aldakheel, F., Raina, A., 2016. Phase field modeling of ductile fracture at finite strains: A variational gradient-extended plasticity-damage theory. International Journal of Plasticity 84, 1 – 32.

Miehe, C., Hofacker, M., Welschinger, F., 2010a. A phase field model for rate-independent crack propagation: Robust algorithmic implementation based on operator splits. Computer Methods in Applied Mechanics and Engineering 199 (45-48), 2765–2778.

Miehe, C., Mauthe, S., 2016. Phase field modeling of fracture in multi-physics problems. part iii. crack driving forces in hydro-poro-elasticity and hydraulic fracturing of fluid-saturated porous media. Computer Methods in Applied Mechanics and Engineering 304, 619–655.

Miehe, C., Welschinger, F., Hofacker, M., 2010b. Thermodynamically consistent phase-field models of fracture: Variational principles and multi-field fe implementations. International Journal for Numerical Methods in Engineering 83 (10), 1273–1311.

Molnár, G., Gravouil, A., 2017. 2d and 3d abaqus implementation of a robust staggered phase-field solution for modeling brittle fracture. Finite Elements in Analysis and Design 130, 27 – 38.

Monchiet, V., Gruescu, C., Cazacu, O., Kondo, D., 2012. A micromechanical approach of crack-induced damage in orthotropic media: application to a brittle matrix composite. Engineering Fracture Mechanics 83, 40–53.

Moës, N., Dolbow, J., Belytschko, T., 1999. A finite element method for crack growth without remeshing. International Journal for Numerical Methods in Engineering 46 (1), 131–150.

Moulinec, H., Silva, F., 2014. Comparison of three accelerated fft-based schemes for computing the mechanical response of composite materials. International Journal for Numerical Methods in Engineering 97, 960–985.

Moulinec, H., Suquet, P., 1994. A fast numerical method for computing the linear and nonlinear mechanical properties of composites. Comptes Rendus de l'Académie des Sciences t.318, 1417–1423.

Moulinec, H., Suquet, P., 1998. A numerical method for computing the overall response of nonlinear composites with complex microstructure. Computer methods in applied mechanics and engineering 157 (1-2), 69–94.

Msekh, M. A., Sargado, J. M., Jamshidian, M., Areias, P. M., Rabczuk, T., 2015. Abaqus implementation of phase-field model for brittle fracture. Computational Materials Science 96, 472 – 484, special Issue Polymeric Composites.

Murari, V., Upadhyay, C., 2013. Micromechanics based diffuse damage model for unidirectional composites. Composite Structures 96, 419–432.

Nguyen, T., Yvonnet, J., Bornert, M., Chateau, C., 2016. Initiation and propagation of complex 3d networks of cracks in heterogeneous quasi-brittle materials: Direct comparison between in situ testing-microct experiments and phase field simulations. Journal of the Mechanics and Physics of Solids 95, 320 – 350.

Nguyen, T.-T., Waldmann, D., Bui, T. Q., 2019. Computational chemo-thermo-mechanical coupling phase-field model for complex fracture induced by early-age shrinkage and hydration heat in cement-based materials. Computer Methods in Applied Mechanics and Engineering 348, 1–28.

Nguyen, V. P., Wu, J.-Y., 2018. Modeling dynamic fracture of solids with a phase-field regularized cohesive zone model. Computer Methods in Applied Mechanics and Engineering 340, 1000 – 1022.

Okubo, S., Fukui, K., 1996. Complete stress-strain curves for various rock types in uniaxial tension. In: International journal of rock mechanics and mining sciences & geomechanics abstracts. Vol. 33. Elsevier, pp. 549–556.

Oskay, C., Fish, J., 2007. Eigendeformation-based reduced order homogenization for failure analysis of heterogeneous materials. Computer Methods in Applied Mechanics and Engineering 196 (7), 1216–1243.

Peerlings, R., Geers, M., De Borst, R., Brekelmans, W., 2001. A critical comparison of nonlocal and gradient-enhanced softening continua. International Journal of solids and Structures 38 (44-45), 7723–7746.

Peerlings, R. H., de Borst, R., Brekelmans, W. M., De Vree, J., 1996. Gradient enhanced damage for quasi-brittle materials. International Journal for numerical methods in engineering 39 (19), 3391–3403.

Pijaudier-Cabot, G., Bazant, Z., 1987. Nonlocal damage theory. Journal of Engineering Mechanics ASCE 113, 1512–1533.

Reis, F., Lopes, I. R., Pires, F. A., Andrade, F., 2018. Microscale analysis of heterogeneous ductile materials with nonlocal damage models of integral type. Computers & Structures 201, 37–57.

Ren, H., Zhuang, X., Anitescu, C., Rabczuk, T., 2019. An explicit phase field method for brittle dynamic fracture. Computers and Structures 217, 45 – 56.

Roth, S.-N., Léger, P., Soulaïmani, A., 2015. A combined xfem–damage mechanics approach for concrete crack propagation. Computer Methods in Applied Mechanics and Engineering 283, 923–955.

Saloustros, S., Cervera, M., Pelà, L., 2019. Challenges, tools and applications of tracking algorithms in the numerical modelling of cracks in concrete and masonry structures. Archives of Computational Methods in Engineering 26 (4), 961–1005.

Sargado, J. M., Keilegavlen, E., Berre, I., Nordbotten, J. M., 2018. High-accuracy phase-field models for brittle fracture based on a new family of degradation functions. Journal of the Mechanics and Physics of Solids 111, 458–489.

Shang, J., Hencher, S., West, L., 2016. Tensile strength of geological discontinuities including incipient bedding, rock joints and mineral veins. Rock Mechanics and Rock Engineering 49 (11), 4213–4225.

Shanthraj, P., Sharma, L., Svendsen, B., Roters, F., Raabe, D., 2016. A phase field model for damage in elasto-viscoplastic materials. Computer Methods in Applied Mechanics and Engineering 312, 167 – 185, phase Field Approaches to Fracture.

Sharma, L., Peerlings, R., Shanthraj, P., Roters, F., Geers, M., 2019. An fft-based spectral solver for interface decohesion modelling using a gradient damage approach. Computational Mechanics, 1–15.

Sharma, L., Peerlings, R. H., Shanthraj, P., Roters, F., Geers, M. G., 2018. Fft-based interface decohesion modelling by a nonlocal interphase. Advanced Modeling and Simulation in Engineering Sciences 5 (1), 1–17.

Shen, W., Shao, J., Liu, Z., Oueslati, A., De Saxcé, G., 2019. Evaluation and improvement of macroscopic yield criteria of porous media having a drucker-prager matrix. International Journal of Plasticity, 102609.

Shen, W., Shao, J., Oueslati, A., De Saxcé, G., Zhang, J., 2018. An approximate strength criterion of porous materials with a pressure sensitive and tension-compression asymmetry matrix. International Journal of Engineering Science 132, 1–15.

Shen, W., Shao, J.-F., Kondo, D., Gatmiri, B., 2012. A micro–macro model for clayey rocks with a plastic compressible porous matrix. International journal of plasticity 36, 64–85.

Simone, A., Askes, H., Sluys, L. J., 2004. Incorrect initiation and propagation of failure in non-local and gradient-enhanced media. International journal of solids and structures 41 (2), 351–363.

Tang, Y., Okubo, S., Xu, J., Peng, S., 2019. Progressive failure behaviors and crack evolution of rocks under triaxial compression by 3d digital image correlation. Engineering geology 249, 172–185.

Ulloa, J., Rodríguez, P., Samaniego, C., Samaniego, E., 2019. Phase-field modeling of fracture for quasi-brittle materials. Underground Space 4 (1), 10 – 21, computational Modeling of Fracture in Geotechnical Engineering Part II.

Vignollet, J., May, S., De Borst, R., Verhoosel, C. V., 2014. Phase-field models for brittle and cohesive fracture. Meccanica 49 (11), 2587–2601.

Wang, Y., Waisman, H., 2016. From diffuse damage to sharp cohesive cracks: A coupled xfem framework for failure analysis of quasi-brittle materials. Computer Methods in Applied Mechanics and Engineering 299, 57–89.

Wells, G. N., Sluys, L., 2001. A new method for modelling cohesive cracks using finite elements. International Journal for Numerical Methods in Engineering 50 (12), 2667–2682.

Wick, T., 2017. Modified newton methods for solving fully monolithic phase-field quasi-static brittle fracture propagation. Computer Methods in Applied Mechanics and Engineering 325, 577 – 611.

Wilson, Z. A., Landis, C. M., 2016. Phase-field modeling of hydraulic fracture. Journal of the Mechanics and Physics of Solids 96, 264–290.

Wu, J.-Y., 2017. A unified phase-field theory for the mechanics of damage and quasi-brittle failure. Journal of the Mechanics and Physics of Solids 103, 72 – 99.

Wu, J.-Y., Huang, Y., 2020. Comprehensive implementations of phase-field damage models in abaqus. Theoretical and Applied Fracture Mechanics 106, 102440.

Zeman, J., Vond?ejc, J., Novák, J., Marek, I., 2010. Accelerating a fft-based solver for numerical homog-

enization of periodic media by conjugate gradients. Journal of Computational Physics 229 (21), 8065 – 8071.

Zeng, Q., Yao, J., Shao, J., 2020. An extended finite element solution for hydraulic fracturing with thermo-hydro-elastic–plastic coupling. Computer Methods in Applied Mechanics and Engineering 364, 112967.

Zeng, Q.-D., Yao, J., Shao, J., 2019. Study of hydraulic fracturing in an anisotropic poroelastic medium via a hybrid edfm-xfem approach. Computers and Geotechnics 105, 51–68.

Zhang, Q., Duan, K., Xiang, W., Yuan, S., Jiao, Y.-Y., 2017. Direct tensile test on brittle rocks with the newly developed centering apparatus. Geotechnical Testing Journal 41 (1), 92–102.

Zhao, L., Zhu, Q., Shao, J., 2018. A micromechanics-based plastic damage model for quasi brittle materials under a large range of compressive stress. International Journal of Plasticity 100, 156–176.

Zhu, Q., Kondo, D., Shao, J., 2009. Homogenization-based analysis of anisotropic damage in brittle materials with unilateral effect and interactions between microcracks. Int. J. for numerical and analytical methods in Geomechanics 33, 749–772.

Zhu, Q., Shao, J., 2017. Micromechanics of rock damage: Advances in the quasi-brittle field. Journal of Rock Mechanics and Geotechnical Engineering 9 (1), 29–40.

Zhu, Q., Shao, J.-F., 2015. A refined micromechanical damage–friction model with strength prediction for rock-like materials under compression. International Journal of Solids and Structures 60, 75–83.

Zhuang, X., Zhou, S., Sheng, M., Li, G., 2020. On the hydraulic fracturing in naturally-layered porous media using the phase field method. Engineering Geology 266, 105306.